Inverse modelling of New Zealand's carbon dioxide balance shows a larger than expected carbon sink

Beata Bukosa

Correspondence: Beata Bukosa (Beata.Bukosa@niwa.co.nz)

S1 Inversion system

We used a Bayesian approach to estimate net air-sea and air-land CO_2 fluxes (Steinkamp et al., 2017; Gurney et al., 2004) for 25 geographic regions (Figure S1). The inversion was based on the Bayesian cost function J, calculated as (Tarantola, 2005):

$$J = \frac{1}{2}(Tx - d)^T C_d^{-1}(Tx - d) + \frac{1}{2}(x - x_0)^T C_0^{-1}(x - x_0) \quad (1)$$

where T is the transport (jacobian) matrix, d is the data time series, x_0 is the prior flux, while C_d and C_0 are the data and prior covariance matrix, respectively. The function was minimized analytically to yield the posterior fluxes (x) and associated posterior error covariance matrix (C) (Enting, 2002) :

$$x = C(T^T C_d^{-1} d + C_0^{-1} x_0) \quad (2)$$

$$C = (T^T C_d^{-1} T + C_0^{-1})^{-1} \quad (3)$$

Equation 1 represents the sum of the modelled versus measured CO_2 differences (Tx - d) and the optimized posterior versus prior flux differences (x - x_0). Each data and flux point is weighted by their uncertainty defined through the data and prior covariance matrix C_d and C_0. The main diagonal of the covariance matrices represents data and prior flux variance while off-diagonal elements contain information about the temporal and spatial correlations of the uncertainties. The first term in Eq. 1 also includes a Gaussian smoother focusing on week-to-week flux changes as described by Steinkamp et al. (2017). We used a reduced chi test ($2J$ divided by the number of observations) (Kountouris et al., 2018) to assess the fit of the inverse model to the observations. The ideal chi-squared value equals 1, with values < 1 indicating that the uncertainties in C_d and/or C_0 are too large while values > 1 suggest that the uncertainties are underestimated (Nickless et al., 2017). Results from the reduced chi test were used as a scaling factor to weight the data uncertainties in the inversion.

S2 Sites, measurements and background

We used hourly mean surface measurements from Baring Head and Lauder, averaged over 13:00 to 14:00 and 15:00 to 16:00 local time, when the air is well-mixed so that the CO_2 signal is representative of regional processes. We have used local

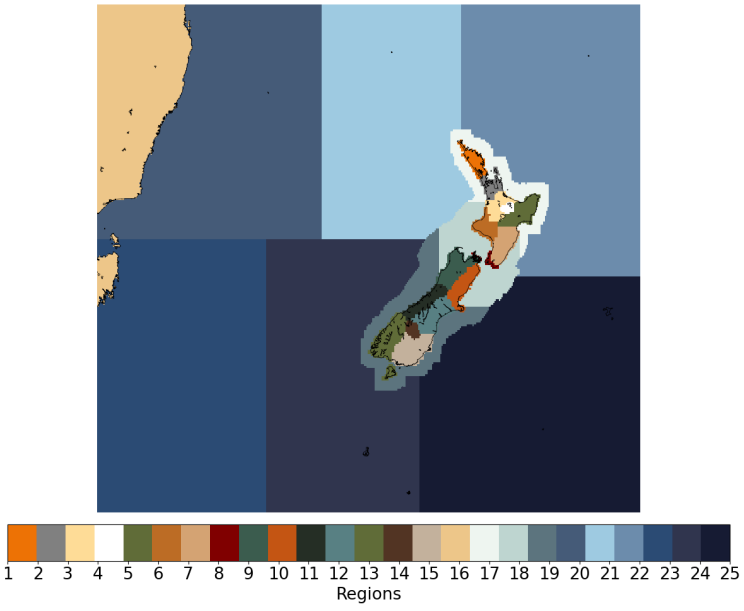

Figure S1. Domain boundaries for the 25 inversion regions, New Zealand South Island (regions 1-8), New Zealand North Island (regions 9-15), Australia (region 16), coastal ocean (regions 17-19), open ocean (regions 20-25).

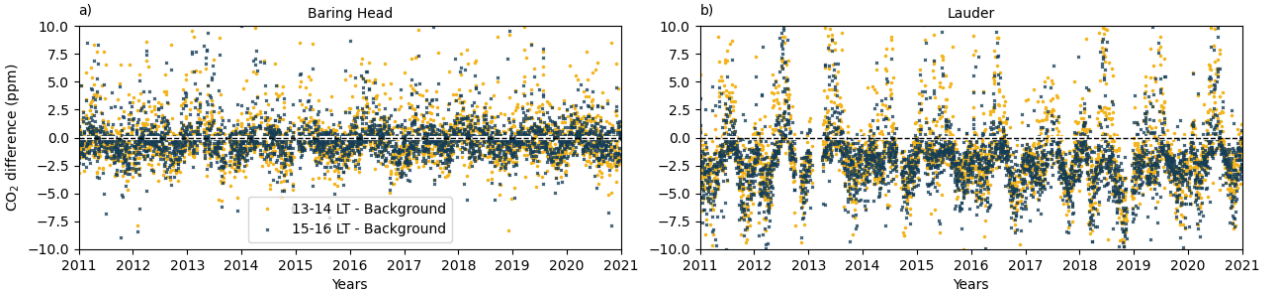

Figure S2. Difference between the 13:00-14:00 (yellow) and 15:00-16:00 (blue) local time CO_2 measurements and the background values at Baring Head (a) and Lauder (b).

time instead of standard local time to account for the shift in hours relative to daylight (i.e., shorter days during winter periods). We excluded data outside of 3 standard deviations of the whole measurement period to remove the influence of local CO_2 processes. The final data for the inversion was constructed by subtracting background measurements from the afternoon measurements at the two sites Fig. S2.

We use a background-sector method to classify the CO_2 background values (Manning, 2011; Steinkamp et al., 2017; Uglietti et al., 2011). Southerly background conditions at Baring Head are present during periods with southerly winds, no land contact and low CO_2 variability (standard deviation < 0.1 ppm, over a minimum of 6 hours) (Stephens et al., 2013), hence can be

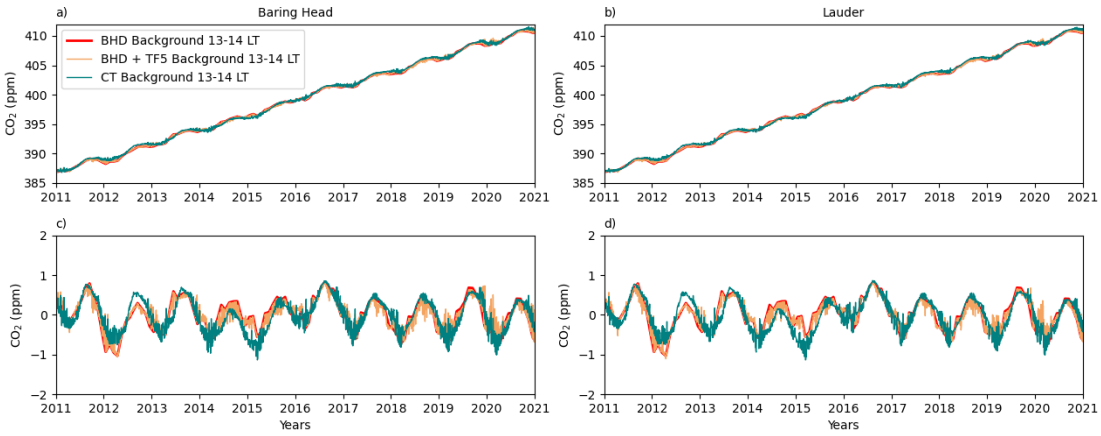

Figure S3. Timeseries of the background values at Baring Head and Lauder at 13-14 local time, estimated from Baring Head baseline values, merged Baring Head and Trans Future 5 ship (TF5) measurements, as well as CarbonTracker CO_2 mole fractions. Plots c and d show the detrended values.

classified as oceanic air (Brailsford et al., 2012). Data points from the TF5 background CO_2 values were selected when the air originated from directions away from coastal regions and typically for regions between 26 and 27°S. Both background data sets had gaps, hence we used the seasonal time series decomposition by the Loess (STL) algorithm to construct a continuous background time series (Cleveland et al., 1990). The two backgrounds were then combined based on modelled back trajectories for 13:00-14:00 and 15:00-16:00 local time at Baring Head and Lauder (Steinkamp et al., 2017). A time series of the detrended background values can be found in Fig. S3. The background CO_2 values were generally higher than measurements collected at 13:00-14:00 and 15:00-16:00 local time (Fig. 2a and Fig. 2b), especially at Lauder, suggesting that overall, New Zealand acted as a CO_2 sink. However, during winter periods we also observed elevated CO_2 values, at both sites, pointing to CO_2 release.

Measurements at Baring Head are from the non-dispersive infrared (NDIR) analyser (Ultramat 3, Siemens, Brailsford et al. (2012)) for the years 2011-2016. In 2016, the instrument was changed to a three-species greenhouse gas cavity ring down spectroscopy analyzer (G2301, Picarro Inc.), and in 2018, the instrument was updated to a four-species analyzer (G2401, Picarro Inc.). The control and calibration procedures described in Brailsford et al. (2012) remained unchanged and were applied for the calibration of each new analyser. The Lauder CO_2 were collected using a dual cell NDIR *in situ* analyser (LI-7000, LI-COR Inc.) with a similar control system as at Baring Head but using nafion drying instead of cryo drying. Baring Head uses a suite of transfer gases provided by the World Meteorological Organization Central Calibration Lab (WMO CCL) at the National Oceanic and Atmospheric Administration (NOAA), while Lauder uses a suite of gases defined at Baring Head against the same transfer suite. Hence the observations are made based on reference gases with the same lineage. To verify the *in situ* observations a suite of four gases from the CCL known as the Aniwaniwa suite are measured as unknowns at each site to assess site specific biases. Sample air at both sites were collected from a 10 m air inlet height. The analysers were calibrated against a suite of standard reference gases with assigned mole fractions on the relevant World Meteorological Organization –

Global Atmosphere Watch (WMO-GAW) scales - the WMO X2019. The Lauder measurements were not directly calibrated to the WMO X2019 scale. We have used the conversion from Equation 6 in Hall et al. (2021) to convert the X2007 to the X2019 scale.

S3 Atmospheric transport model

In our inversion, we used the NAME III vn6.5 dispersion model for the years 2014-2020 while for the period 2011-2013, we retained the original NAME III vn6.1 simulations previously described in Steinkamp et al. (2017) (Fig. S4). We used NIWA's operational NZLAM fields for the years 2011-2013 and NZCSM data for the period from mid-2016 to 2020. NAME III required input data that was not routinely generated by NZCSM for the period 2014 to mid-2016. For this period, we therefore configured a NZCSM-like model workflow that was run in hindcast mode, creating NAME III input fields for the 2014 to mid-2016 period.

Both NZLAM and NZCSM are New Zealand specific configurations of the UK Met Office Unified Model (UM) (Davies et al., 2005) and use the same semi-implicit semi-Lagrangian dynamical core, called "ENDGame" (Wood et al., 2014), but they differ in their domain size, horizontal (Fig. S5) and vertical resolutions, as well their scientific configurations. NZLAM provides meteorological outputs on a 324x324 grid point ≈12 km horizontal resolution with hourly forecast output resolution, while NZCSM operates at a finer 1200x1350 grid point, ≈1.5 km spatial resolution, generating 30-minute temporal resolution output. Both models utilise 70 vertical levels, with NZLAM extending to 80 km above the surface and NZCSM to 40 km. NZCSM thereby achieves a higher resolution through the boundary layer and lower troposphere. We note that the NZCSM model from the mid 2016 to mid 2017 period was based on the "pre-ENDGAME" version of the model.

To creata the NZCSM-like meteorological input, UK Met Office Global model analyses were retrieved for 00Z for each day in the re-run period. A N768 horizontal resolution (approximately 17km at mid-latitudes) UM Global model forecast, running the GA6.1 science configuration (Walters et al., 2017) was run for 30 hours, outputting at hourly intervals lateral boundary condition data for a one-way nested ≈12 km resolution NZLAM-like regional model. This model also used the GA6.1 science configuration, which was very similar to the operational NZLAM model of the time and was also run for 30 hours, with lateral boundary condition data generated to drive a one-way nested NZCSM-like ≈1.5 km horizontal resolution regional model. The science configuration used in this ≈1.5 km resolution model was the mid-latitude Regional Atmosphere 2 (RAL2-M) set-up favoured by convection-resolving regional UM configurations, featuring minor changes to the RA1-M configuration described in Bush et al. (2020). This nesting set-up mirrored the operational nesting of the NZLAM and NZCSM model of the time. Both regional models were configured to output all necessary data to force a NAME III simulation. To allow for model spin-up, the first 6 hours of each forecast were ignored when constructing a continuous time series of data from which the NAME III simulations were run.

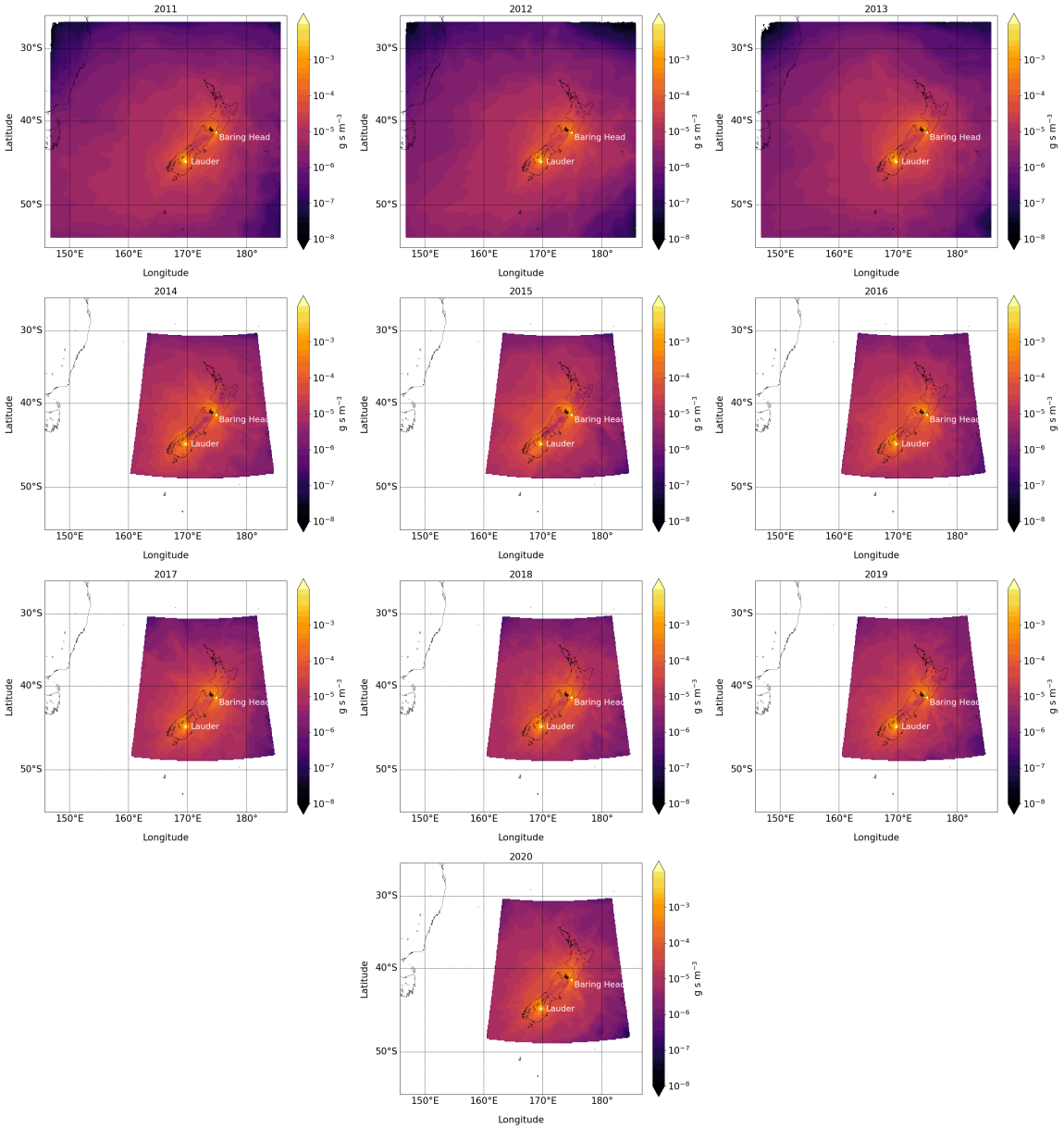

Figure S4. Combined NAME III footprints based on Baring Head and Lauder for each year in 2011-2020 at 13-14 and 15-16 local release time. 2011-2013 footprints are based on NZLAM while 2014-2020 is based on NZCSM meteorology input.

S3.1 Atmospheric transport model comparison

In addition to the wind speed and direction (Fig. S7) we also compare the height of measured Planetary Boundary Layer (PBL) at Lauder with modelled values (Fig. S6). The PBL dataset is based on radiosonde measurements as described in (Steinkamp

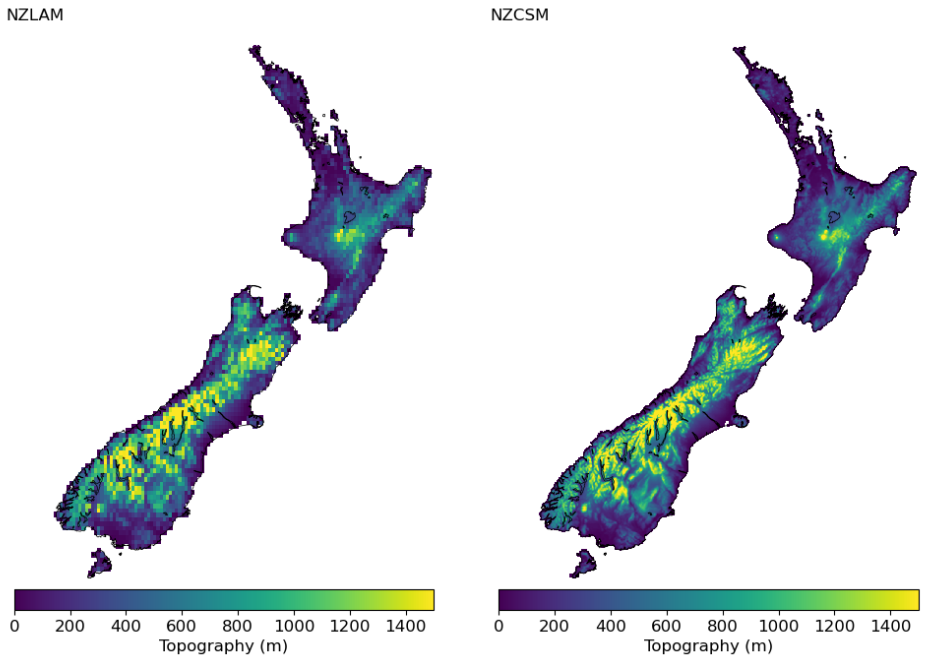

Figure S5. New Zealand's Topography in the NZLAM and NZCSM model.

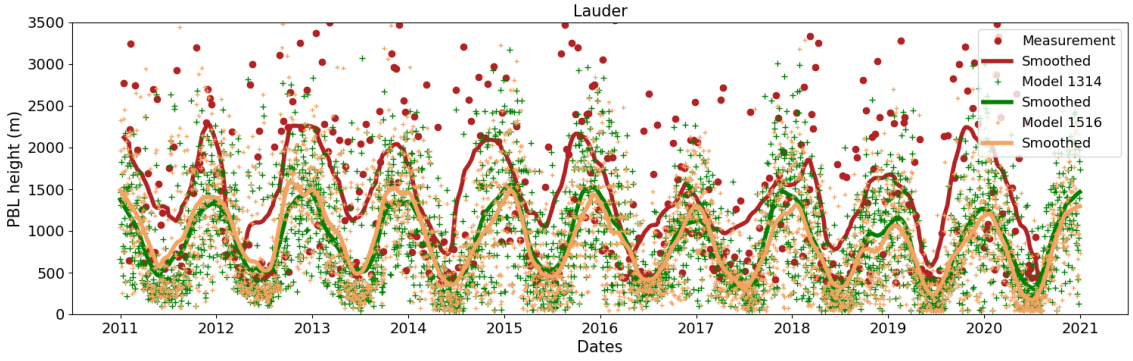

Figure S6. Measured (red) and modelled (orange and green) Planetary Boundary Layer (PBL) height at Lauder. Modelled values are based on 13:00-14 :00 and 15:00-16:00 local time. The measurements are from radiosonde observations and are shown for all available data throughout the day. Lines represent the smoothed estimates of the measured and modelled data.

et al., 2017). Over or underestimated PBL in the model could lead to further biases in the estimated fluxes. The modelled PBL heights are lower than the measurements during the whole inversion period, resulting in a shallower PBL. A shallower PBL and limited vertical mixing could lead to amplified modelled CO_2 mole fractions which could reduce the estimated CO_2 uptake. We have found that all models underestimated the measured PBL.

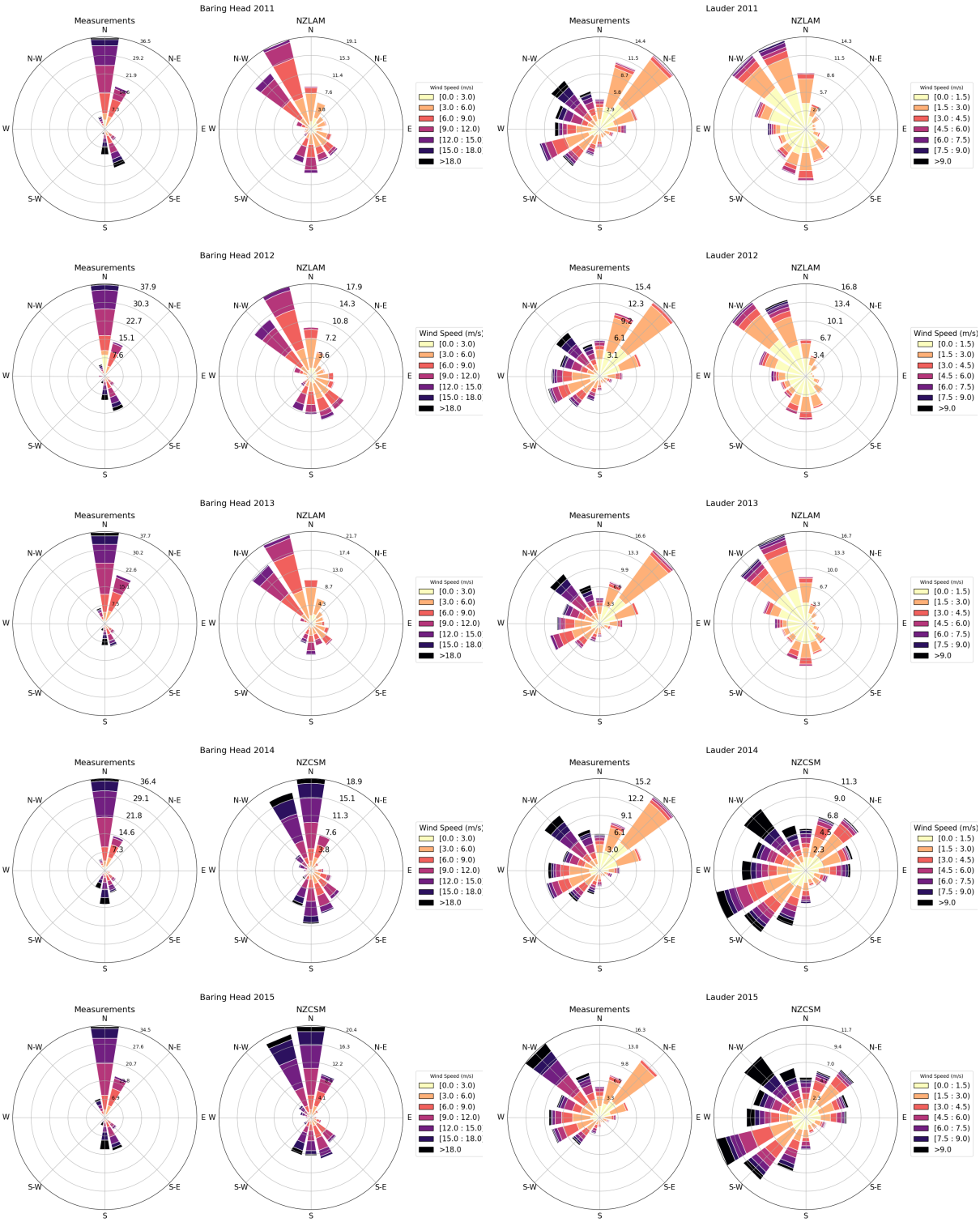

Figure S7. Annual modelled and measured wind roses at Baring Head and Lauder.

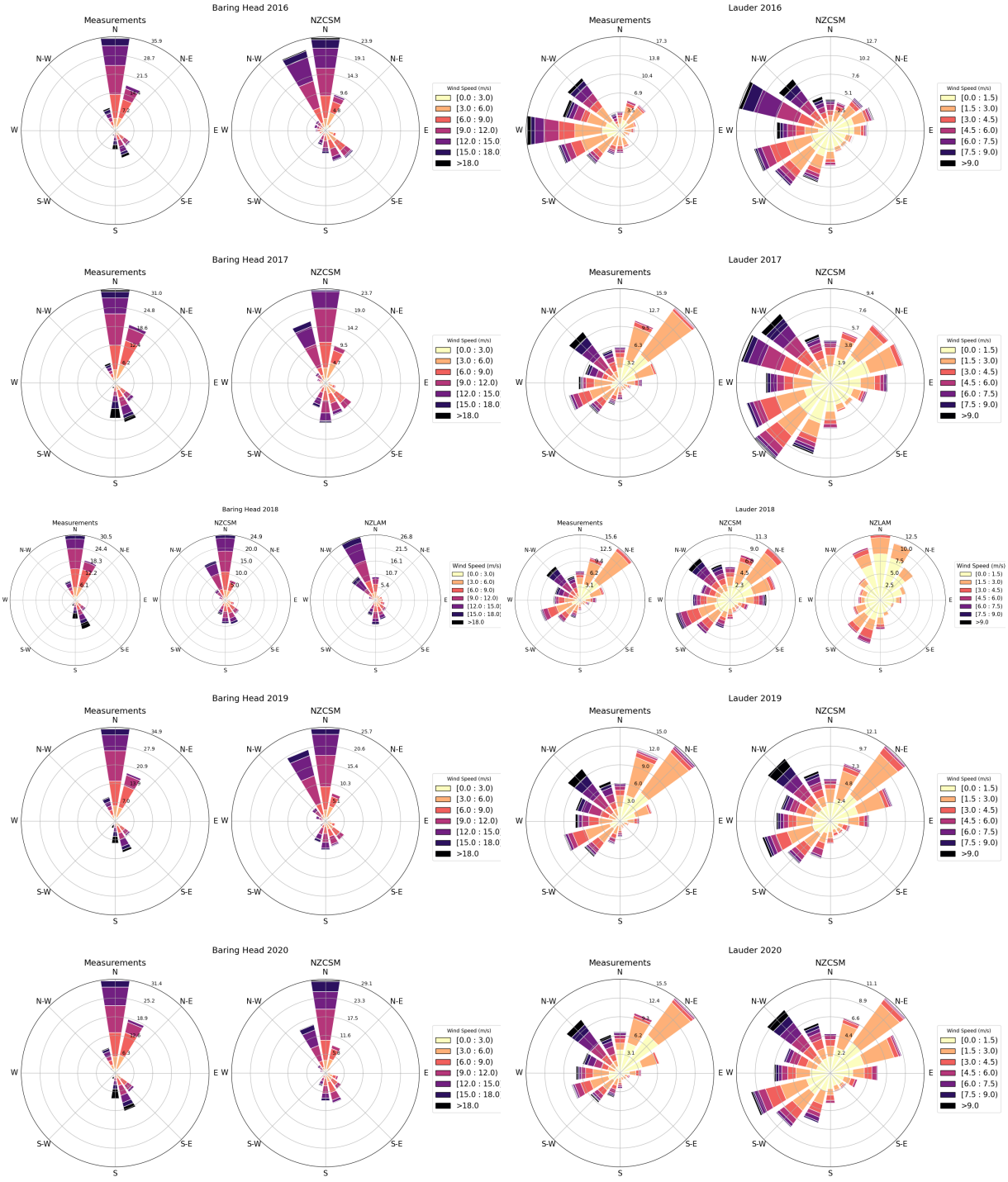

Figure S7. Continued. Annual modelled and measured wind roses at Baring Head and Lauder.

S4 Prior ocean fluxes

The prior oceanic fluxes in our inversion domain were extracted from monthly global open-ocean air-sea CO_2 fluxes (Landschützer et al., 2016, 2020a). The product from Landschützer et al. (2020a) does not provide fluxes for coastal areas. We therefore merged the open-ocean fluxes with coastal fluxes calculated from the climatology of ocean surface coastal pCO_2 (Landschützer et al., 2020b).

We used year-specific monthly open-ocean CO_2 fluxes up to 2019 (Landschützer et al., 2020a) while for year 2020 we calculated the CO_2 fluxes from 2019 pCO_2 data following the method from Landschützer et al. (2016):

$$F_{CO_2} = k_w \cdot S_{CO_2} \cdot (1 - f_{ice}) \cdot (pCO_2 - pCO_2^{atm}) \tag{4}$$

where F_{CO_2} represent the resulting monthly air-sea flux of CO_2 in mol C m^{-2} yr^{-1}, k_w refers to the gas transfer velocity of CO_2 calculated based on (Sweeney et al., 2007):

$$k_w = 0.27 \cdot (\frac{S_c}{660})^{-\frac{1}{2}} \cdot u^2 \tag{5}$$

where S_c represents the dimensionless Schmidt number (Wanninkhof, 1992), estimated from year-specific (2011-2020) ERA5 monthly sea surface temperature (Hersbach et al., 2019) and u is the monthly mean wind speed from year specific hourly ERA5 wind fields at a height of 10 m above the sea surface (Hersbach et al., 2018). In Eq. 4 S_{CO_2} is the solubility of CO_2 in seawater calculated according to Weiss (1974) using the same ERA5 temperature fields as for the S_c calculation and annual climatology salinity fields from CARS (CSIRO Atlas of Regional Seas, (CARS, 2009)), f_{ice} is the ice cover. However, since the flux calculation was only performed for our inversion domain that is ice-free we assume f_{ice} = 0, pCO_2 is the sea surface partial pressure taken from Landschützer et al. (2020a) for the coastal fluxes and Landschützer et al. (2016) for the 2020 open-ocean fluxes while pCO_2^{atm} represents the partial pressure of atmospheric CO_2 estimated from the baseline dry air mixing ratio xCO_2 at Baring Head and taking into account the water vapor correction according to Dickson et al. (2007):

$$pCO_2^{atm} = xCO_2 \cdot (P_{atm,surf} - P_{H_2O}) \tag{6}$$

where $P_{atm,surf}$ is the mean sea level pressure from monthly ERA5 fields (Hersbach et al., 2019) and P_{H_2O} describes the water vapour pressure (Weiss and Price, 1980).

The 2019 pCO_2 values used for the calculation of the 2020 CO_2 fluxes were additionally extrapolated to the year 2020 based on the 2011-2019 trend of pCO_2. The trend was estimated from monthly average pCO_2 values inside of the inversion domain. We used the same method for the calculation of the coastal CO_2 fluxes. Since the coastal pCO_2 values were based on climatological data, we also scaled the monthly climatology values based on the open-ocean pCO_2 trend.

S5 Biome-BGCMuSo, calibration for New Zealand pasture systems

We calibrated 18 ecophysiological model parameters for New Zealand pasture systems ("dairy" and "sheep and beef" biomes) using eddy covariance (EC) data from five sites across New Zealand, with an additional five sites available for validation. All sites had at least one full year of data available, and many had three years or more. The parameters were optimized to produce the best match between observed and modelled weekly mean net ecosystem production (NEP), gross primary production (GPP), Ecosystem Respiration (ER), evapotranspiration (ET), and 10 cm soil moisture content (SMC) using the PEST software package: https://dev-sspa-pest.pantheonsite.io/ (Doherty, 2015). Overall, the model achieved a correlation coefficient R^2 of 0.34 and root mean square error (RMSE) of 1.89 g C m^{-2} day^{-1} at the calibration sites, and 0.37 and 2.01 at the validation sites for modelled NEP against observations. However, these metrics varied significantly among sites, and R^2 for components of NEP (GPP and ER) is higher (0.48 and 0.37, respectively). A full description of the calibration methodology and results are the subject of a forthcoming paper (Keller et al. in prep). Note, in the inversion we are using net ecosystem exchange (NEE) fluxes which are obtained from NEP fluxes (same as NEE but with opposite sign depending on disciplinary convention).

The main difference between the "dairy" and "sheep/beef" systems is the intensity of grazing and the use of fertiliser and irrigation. Dairy farm systems in New Zealand are generally intensely grazed (mean stocking rate of 2.86 cows per hectare in 2020-21; Livestock Improvement Corporation and Dairy NZ (2021)) and fertilised and/or irrigated as needed. The model simulated a stocking rate of 3.0 livestock units (LSU) per hectare for dairy at a weight of 420 kg per LSU and 6.0 LSU per hectare for sheep/beef with weight of 55 kg per LSU. Grazing was simulated by designating one week of grazing and leaving the following three weeks idle during spring, summer, and autumn. No grazing occurred during the winter months (June, July and August). Four different grazing rotations were simulated for each pixel, each offset by one week. Fluxes from each rotation were then averaged to produce a mean value for the pixel. Nitrogen fertiliser was applied twice per year in September and March in dairy systems. Irrigation was simulated for dairy systems in areas where data indicates irrigation is in use (MfE, 2017) . Sheep/beef systems received no fertiliser or irrigation in our simulations. The other Biome-BGCMuSo biomes (ungrazed grassland, shrub, and evergreen broadleaf forest, evergreen needleleaf forest) were not parameterized for New Zealand due to lack of suitable data. Model default parameters were used. Parameter files can be downloaded from the Biome-BGCMuSo website (https://nimbus.elte.hu/bbgc/). The final monthly contribution of the fluxes are shown in Fig. S8.

S5.1 Land cover

The dataset that was used to determine the land cover type for the prior was derived from the New Zealand Land Cover Database (LCDB) v5.0 (Landcare Research, 2020). Each of the LCDB categories was first mapped into five broad categories to construct the prior (Table S1). The grassland category was further disaggregated into dairy, sheep/beef, or ungrazed subcategories based on the LUCAS Land Use Map (MfE, 2016) and further analysis (Manderson et al., 2019) that used a fuzzy logic framework to improve the classification of low- and high-producing grassland and to assign a general farm class (dairy, other livestock, and ungrazed/not otherwise used for agriculture). The area of each category within each VCSN grid cell was translated into a percentage coverage. The land type with the largest percentage was considered the dominant land type and the whole grid cell

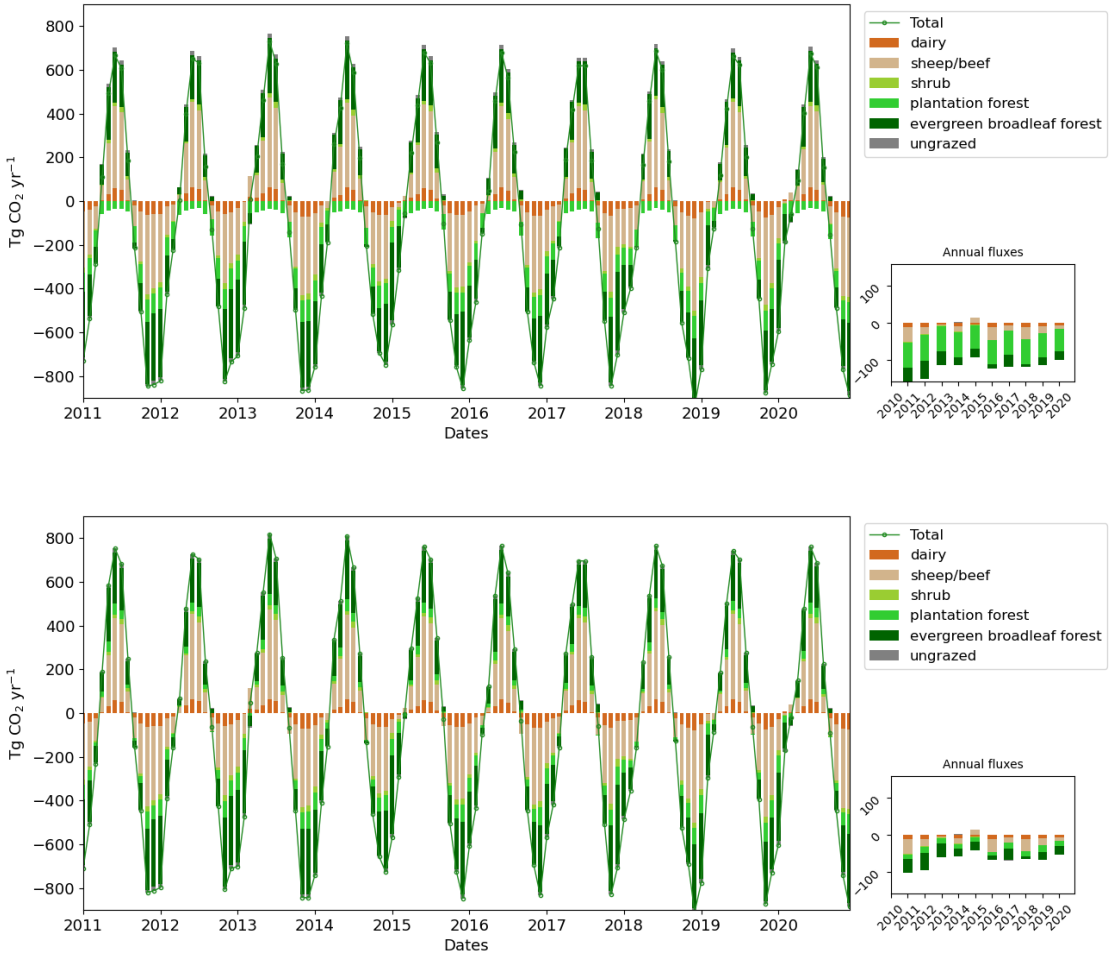

Figure S8. Monthly and annual contribution of the fluxes based on the Biome-BGCMuSo biomes and CenW (top plot) and Biome-BGCMuSo (bottom plot).

was set to that category. This resulted in 12 categories (Table S2) that were grouped into a final 10 category map following the categories in Steinkamp et al. (2017) and matched with the Biome-BGCMuSo biomes (dairy pasture, sheep/beef pasture, ungrazed grassland, shrub, evergreen broadleaf forest (EBF), and evergreen needleleaf forest (ENF)). In our base inversion, the exotic forest category (i.e., ENF) was modelled using *Pinus radiata* fluxes from the CenW mode; however, we also performed inversion sensitivity tests to quantify the impact of Biome-BGCMuSo ENF on our results.

Table S1. Land cover category merging and mapping in Biome-BGCMuSo.

LCDB v5.0 category	Prior category
MANUKA AND / OR KANUKA SUB-ALPINE SHRUBLAND MATAGOURI OR GREY SCRUB MIXED EXOTIC SHRUBLAND GORSE AND / OR BROOM FLAXLAND FERNLAND	Shrub
LOW-PRODUCING GRASSLAND DEPLETED GRASSLAND HIGH-PRODUCING EXOTIC GRASSLAND TALL TUSSOCK GRASSLAND ALPINE GRASS HERBFIELD GRASS OTHER	Grassland (subcategories: dairy, sheep/beef, ungrazed)
EXOTIC FOREST FOREST HARVESTED	Exotic forest (*Pinus radiata* or ENF)
BROADLEAVED INDIGENOUS HARDWOODS DECIDUOUS HARDWOODS INDIGENOUS FOREST	Indigenous forest (EBF)
OTHERS NOT LISTED	Other (zero or non-existing prior flux)

Table S2. Final land cover category merging and mapping.

Prior category	Final Category	Assigned flux
Shrub	Scrub and Shrubland	Biome-BGCMuSo v6.1 dairy pasture
Dairy grassland	Grassland: Dairy pasture	Biome-BGCMuSo v6.1 sheep and beef pasture
Sheep/Beef grassland	Grassland: Sheep/Beef pasture	Biome-BGCMuSo v6.1 shrub
Ungrazed grass	Grassland: Other	Biome-BGCMuSo v6.1 ungrazed grassland
Exotic forest	Forest: Plantation	CenW *Pinus radiata*
Indigenous forest	Forest: Other	Biome-BGCMuSo v6.1 evergreen broadleaf forest (EBF)
Cropland	Cropland	Set to non-existing*
Freshwater vegetation	Bare or Lightly-vegetated Surfaces	Set to zero*
Saline vegetation	Bare or Lightly-vegetated Surfaces	Set to zero*
No vegetation	Bare or Lightly-vegetated Surfaces	Set to zero*
Urban	Artificial Surfaces	Set to zero*
Water	Water Bodies	Set to zero*

*Note these categories at not modelled in Biome-BGCMuSo hence we assign a zero flux or set it as non-existing (NaN)

Table S3. Total area of each region and land type proportion in %

Region	Artificial Surfaces	Bare or Lightly vegetated Surfaces	Water Bodies	Cropland	Grassland: Dairy pasture	Grassland: Sheep/Beef pasture	Grassland: Other	Scrub and Shrubland	Forest Plantation	Forest Other	Area (m2)	Area (ha)
1	0.12	0.37	0.0	0.0	7.27	34.61	0.12	3.45	7.64	11.21	20529072611.63	2052907.26
2	3.51	0.15	0.15	0.15	11.11	28.95	0.44	2.63	3.51	11.4	16780887356.77	1678088.74
3	0.38	0.26	3.33	0.51	24.87	38.08	0.0	0.13	4.62	17.95	19072300202.87	1907230.02
4	0.48	0.0	3.85	0.0	20.19	21.63	0.0	0.48	42.79	10.58	5049118787.61	504911.88
5	0.24	0.49	0.57	0.49	1.38	27.12	1.79	4.07	15.72	34.36	29778444837.37	2977844.48
6	0.25	0.0	0.0	0.0	14.32	26.76	0.75	0.5	2.64	34.42	19070144794.56	1907014.48
7	0.52	0.0	0.26	1.03	4.48	63.45	1.12	3.79	3.53	11.64	27296523600.79	2729652.36
8	4.63	0.0	0.46	0.0	0.46	12.5	0.46	8.33	0.46	15.74	5075744524.94	507574.45
9	0.16	1.18	0.08	0.39	2.51	5.25	3.84	0.94	5.56	63.32	29505096893.63	2950509.69
10	0.87	2.51	0.29	2.22	1.74	47.68	14.86	5.79	2.22	7.14	23554739296.96	2355473.93
11	0.0	20.02	0.43	0.0	2.6	6.82	13.96	1.62	0.65	41.88	20895528028.29	2089552.8
12	0.08	1.93	2.17	5.39	8.04	62.3	11.74	0.24	0.88	0.64	27629717909.83	2762971.79
13	0.0	2.43	2.0	0.0	0.3	13.17	17.05	1.7	0.42	41.81	35788733444.43	3578873.34
14	0.0	0.34	6.08	0.0	0.34	80.07	11.82	0.0	0.0	1.35	6523169736.95	652316.97
15	0.14	0.42	0.07	0.0	6.57	68.86	4.87	0.42	4.31	4.31	30510835736.26	3051083.57

S6 Lateral transport and fjords

Lateral transport, erosion and deposition of organic material can be very important in montane regions and other steeplands when accompanied by rapid re-establishment of productive vegetation on the disturbed landscape (Stallard, 1998; Berhe et al., 2018). Episodic events associated with precipitation and tectonic activity induce landslides in the Fiordland/West Coast regions. Quantification of sediment flux from landslides(Hovius et al., 1997) has not been extended to carbon, but could be substantial (Bianchi et al., 2020). However, these processes would not account for similar sink sizes in flatter land with lower rainfall, e.g., Southland. Globally, fjords such as those found on the southwest coast of New Zealand are known to be hotspots for organic carbon buria (Smith et al., 2015). We observe that regions such as Fiordland and Westland (Southern Alps) provide ideal conditions for erosion and burial as net carbon sinks, expanding on other published work (Scott et al., 2006; Dymond, 2010). A critical pre-conditioning of the sink potential is provided by the rapid colonisation of disturbed landslides and debris by the prolific nitrogen-fixer Coriaria arborea. This species dominates for as long 20-30 years after disturbance, with nitrogen-fixation estimates ranking among the highest observed internationally (Silvester, 1976). Rapid nitrogen accumulation is expected to drive optimal photosynthetic rates in Fiordland's and Westland's cool, year-round maritime climate (Silvester, 1976), which are known to exceed those used historically in successional models of New Zealand forest (Hall, 2001). Models such as Biome-BGCMuSo can account for nitrogen fixation and elevated nitrogen levels but our simulations do not include land disturbance and the succession of nitrogen-fixing grasses to mature forest. This leads to a potential bias in carbon fluxes in disturbed landscapes, missing the rapid accumulation of carbon accompanied by burial. The erosion processes are highly non-linear, requiring special treatment. Nevertheless, hydrologic scaling models (Scott et al., 2006) or fractal landslide models for erosion rates (Hovius et al., 1997) could enable correction terms to be incorporated into priors used for Observing System Simulation Experiment (OSSE) or final estimation in future studies.

Lateral transport of carbon in rivers in the form of dissolved organic carbon (DOC), dissolved inorganic carbon (DIC), and particulate organic carbon (POC) can be substantial (Lauerwald et al., 2023). The flux of DOC from any land area can represent a localised carbon sink from the atmospheric perspective but may be neutralised if respired following hydrologic transfers to downstream environments. While a substantial amount of CO_2 is emitted to the atmosphere during transport (Lauerwald et al., 2023), some of this carbon is exported to coastal systems and the ocean. The recent Australasia regional carbon budget assessment Villalobos et al. (2023) estimated that rivers over the whole of New Zealand transport on average 5.5 $\pm$ 2.6 Tg CO_2 yr^{-1} of DOC, 4 $\pm$ 2.2 Tg CO_2 yr^{-1} POC and 5.1 $\pm$ 2.6 Tg CO_2 yr^{-1} DIC (including the flux from weathering) to estuaries and coastal wetlands. The same study estimated a net flux of 2.2 $\pm$ 1.1 Tg CO_2 yr^{-1} from New Zealand's rivers to the atmosphere. After further exchange with the atmosphere through coastal vegetation and estuaries, 8.8 $\pm$ 15.4 Tg CO_2 yr^{-1} eventually makes its way to the continental shelves in the ocean. This is not spread evenly over all regions, as some regions have more river surface area than others, and fluxes in individual catchments and different environments can vary widely. Other studies have estimated that riverine export of DOC and POC is significant at 4 $\pm$ 1.1 Tg CO_2 yr^{-1} and 9.9 $\pm$ 3.6 Tg CO_2 yr^{-1} (Scott et al., 2006), and the majority of this export is happening along the South Island's West Coast, Southern Alps and Fiordland (Scott et al., 2006; McGroddy et al., 2008; Dymond, 2010), including certain regions where our results

indicate stronger CO_2 removal from the atmosphere (Fiordland region -39 $\pm$ 10 Tg CO_2 yr^{-1}, Fig. 9). These studies suggest topography, drainage, vegetation type, and lithology are important controls and agree adequately with intensive catchment scale studies (Moore, 1989).

Fjords and other coastal ecosystems are thought to be overall global carbon sinks. In particular, fjords are important sinks, absorbing much more carbon per unit area than other coastal and estuarine environments. Globally, fjords comprise about 0.1% of the ocean surface area and account for 11% of carbon sequestered into ocean sediment (Smith et al., 2015). The sparse data suggest that Fiordland's fjords have some of the highest carbon sequestration rates of any fjords globally (Bianchi et al., 2020). Using global median estimates (-0.12 kg CO_2 m^{-2} yr^{-1}, Rosentreter et al. (2023)) and an estimated total surface area of 779 km^2, New Zealand's fjords are a sink of -0.097 Tg CO_2 yr^{-1} (Rosentreter et al., 2023; Villalobos et al., 2023). This would only explain a very small portion of the sink that we infer from the inversion. However, the global average is partly derived from measurements taken at high latitudes in Europe and North America, where fjords are mostly or entirely glaciated. There is evidence that New Zealand fjords have high rates of organic carbon burial (Ramirez et al., 2016) relative to glaciated fjords in other parts of the world due to vegetation, temperate climate and frequent, heavy rainfall. We expect that CO_2 fluxes from New Zealand's fjords would be at the higher end of the range of that observed globally, but more local observations are needed to verify this, and the bottom-up CO_2 uptake (Rosentreter et al., 2023; Villalobos et al., 2023) would have to be an order of magnitude greater to make a 5% contribution to the observed sink in Fiordland.

Table S4. Annual prior and posterior regional flux estimates with uncertainties and 2011-2020 average values in units of Tg CO_2 yr^{-1}.

	Prior											Post										
Region	2011	2012	2013	2014	2015	2016	2017	2018	2019	2020	2011-2020	2011	2012	2013	2014	2015	2016	2017	2018	2019	2020	2011-2020
Fluxes																						
1	-13.71	-10.95	-4.85	-11.78	-9.01	-12.29	-7.04	-11.75	-8.74	-4.08	-9.42	-12.25	-9.86	-4.04	-11.89	-7.97	-9.4	-6.74	-12.58	-7.55	-4.09	-8.64
2	-8.05	-6.89	-2.83	-7.43	-4.53	-5.55	-3.06	-6.74	-6.17	-2.11	-5.34	-6.38	-5.45	-2.21	-7.14	-3.54	-2.99	-2.43	-6.33	-5.16	-1.97	-4.36
3	-11.78	-12.09	-5.61	-8.36	-7.01	-9.28	-7.5	-10.47	-10.45	-6.68	-8.92	-4.76	-7.75	-3.97	-8.49	1.05	-0.1	-6.88	-9.11	-12.16	-9.35	-6.15
4	-11.07	-11.48	-10.1	-10.92	-9.86	-10.47	-9.97	-10.69	-10.69	-9.35	-10.46	-10.5	-11.17	-9.87	-10.67	-9.63	-10.09	-9.96	-10.39	-10.97	-9.5	-10.28
5	-26.56	-32.51	-27.43	-31.02	-27.08	-26.8	-27.34	-27.82	-28.38	-27.46	-28.24	-22.94	-28.47	-26.51	-29.85	-21.11	-22.04	-25.77	-18.62	-28.87	-30.48	-25.47
6	-8.57	-9.48	-6.72	-4.45	-3.6	-4.01	-6.08	-4.95	-7.6	-5.24	-6.07	1.4	-2.02	-1.63	-1.58	10.74	4.03	-1.93	-4.67	-8.55	-1.58	-0.58
7	-9.0	-10.74	-5.96	-10.75	-1.17	-8.4	-9.6	-9.65	-12.14	-2.78	-8.02	0.92	-6.95	-3.72	-6.36	3.0	-2.43	-4.47	-6.4	-12.65	-6.43	-4.55
8	-0.62	-1.06	-0.41	-1.05	-0.27	-0.26	-0.75	-0.35	-0.57	-0.03	-0.54	0.06	0.05	-0.46	-1.29	-0.03	0.76	0.66	0.38	-0.18	-0.43	-0.05
9	-21.36	-20.1	-17.41	-12.83	-9.39	-10.81	-17.91	-12.59	-11.99	-15.19	-14.96	-32.34	-28.07	-19.83	-25.35	-24.61	-25.58	-31.68	-23.94	-23.39	-18.81	-25.36
10	-4.68	-3.92	-1.91	-1.56	4.49	-4.55	-2.92	-7.41	-2.3	-2.94	-2.77	4.29	2.98	3.17	1.22	5.24	-2.58	-1.95	0.63	8.49	-0.81	2.07
11	-8.69	-8.64	-7.34	-2.78	-6.13	-4.26	-6.93	-2.44	-0.81	-3.84	-5.19	-18.37	-11.15	-9.01	-4.08	-7.52	-13.9	-15.54	-8.39	-14.6	-12.0	-11.46
12	-11.4	-4.19	-1.79	-1.16	3.08	-10.81	-3.27	-7.46	-3.58	-6.12	-4.67	-12.01	-5.21	0.0	-4.54	3.75	-9.67	-11.52	-5.75	-2.02	-11.37	-5.83
13	-8.22	-9.46	-7.41	-0.41	-4.06	-2.47	-6.85	4.54	1.98	-3.95	-3.63	-53.38	-32.04	-22.73	-36.09	-36.92	-53.88	-52.13	-40.76	-32.56	-28.48	-38.9
14	-3.2	-0.44	-0.23	0.94	0.03	-1.49	-0.23	-0.26	-1.29	-0.86	-0.7	-9.75	-6.48	-4.71	-6.69	-4.43	-7.83	-6.73	-9.84	-8.79	-6.18	-7.14
15	-14.59	-8.42	-8.7	-9.22	-3.41	-10.38	-11.17	-7.44	-11.71	-10.39	-9.54	-23.9	-8.47	-15.69	-36.07	-26.89	-23.45	-28.48	-38.95	-17.73	-23.47	-24.31
Uncertainties																						
1	5.43	5.34	5.16	5.19	5.24	5.56	5.32	5.52	5.44	5.11	5.33	5.37	5.3	5.12	5.16	5.19	5.47	5.26	5.4	5.25	5.05	5.26
2	4.27	4.15	4.07	4.06	4.04	4.19	4.05	4.16	4.15	3.88	4.1	4.2	4.1	4.03	4.02	3.99	4.13	4.0	4.05	4.06	3.79	4.04
3	6.6	6.43	6.4	6.17	6.21	6.45	6.37	6.46	6.48	6.26	6.38	6.32	6.13	6.23	5.85	6.01	6.14	6.15	6.12	6.08	5.77	6.08
4	2.25	2.19	2.17	2.16	2.12	2.2	2.16	2.21	2.21	2.12	2.18	2.2	2.16	2.14	2.12	2.06	2.16	2.1	2.17	2.16	2.07	2.13
5	12.71	12.25	12.51	12.19	12.15	12.45	12.4	12.52	12.56	12.36	12.41	12.38	11.91	12.22	11.86	11.82	11.96	11.86	11.89	12.05	11.88	11.98
6	7.62	7.29	7.55	7.03	7.03	7.15	7.07	7.05	7.19	6.98	7.2	6.54	6.65	6.83	6.47	6.48	6.39	5.94	5.87	5.94	5.3	6.24
7	8.36	8.17	8.23	7.92	7.7	8.02	8.09	8.21	8.21	7.86	8.08	7.47	7.06	7.45	7.42	7.3	6.91	7.03	6.68	7.22	6.67	7.12
8	1.2	1.19	1.24	1.19	1.14	1.18	1.17	1.19	1.18	1.15	1.18	1.02	1.04	1.08	0.93	0.8	0.85	0.82	0.85	0.89	0.82	0.91
9	14.38	13.66	13.8	12.7	12.55	12.86	12.82	12.92	12.55	12.73	13.1	11.0	10.14	10.25	10.72	10.68	9.22	8.39	8.84	7.81	8.45	9.55
10	6.32	6.13	6.29	5.82	5.36	5.85	5.88	6.29	6.01	5.86	5.98	5.67	5.6	5.86	5.55	4.99	5.51	5.37	5.93	5.56	5.33	5.54
11	6.93	6.82	6.89	6.19	6.39	6.3	6.18	6.07	5.77	5.87	6.34	6.16	5.85	6.4	5.06	5.2	5.26	5.0	5.32	4.98	5.0	5.42
12	6.23	5.92	5.8	5.38	5.02	5.89	5.76	6.46	5.98	5.69	5.81	5.24	5.24	5.44	5.06	4.6	5.5	5.12	5.8	5.49	5.04	5.25
13	13.03	12.63	12.8	11.53	11.68	11.45	11.15	10.7	10.34	10.6	11.59	11.1	10.08	11.43	8.38	8.88	9.03	8.16	8.7	8.0	7.79	9.15
14	1.65	1.5	1.46	1.32	1.31	1.46	1.39	1.54	1.51	1.46	1.46	0.87	0.88	1.08	0.93	1.03	0.98	0.91	1.0	0.96	0.88	0.95
15	9.08	8.64	8.64	8.53	8.26	8.6	8.62	8.94	8.87	8.72	8.69	6.78	7.12	7.44	6.98	6.89	6.62	6.34	6.93	6.34	5.92	6.74

Table S5. Annual prior and posterior regional flux estimates with uncertainties and 2011-2020 average values in units of t C ha^{-1} yr^{-1}.

	Prior											Post									
Region	2011	2012	2013	2014	2015	2016	2017	2018	2019	2020	2011-2020	2011	2012	2013	2014	2015	2016	2017	2018	2019	2020	2011-2020
Fluxes																						
1	-1.82	-1.45	-0.64	-1.56	-1.2	-1.63	-0.94	-1.56	-1.16	-0.54	-1.25	-1.63	-1.31	-0.54	-1.58	-1.06	-1.25	-0.9	-1.67	-1.0	-0.54	-1.15
2	-1.31	-1.12	-0.46	-1.21	-0.74	-0.9	-0.5	-1.1	-1.0	-0.34	-0.87	-1.04	-0.89	-0.36	-1.16	-0.58	-0.49	-0.39	-1.03	-0.84	-0.32	-0.71
3	-1.68	-1.73	-0.8	-1.2	-1.0	-1.33	-1.07	-1.5	-1.49	-0.95	-1.28	-0.68	-1.11	-0.57	-1.21	0.15	-0.01	-0.98	-1.3	-1.74	-1.34	-0.88
4	-5.98	-6.2	-5.46	-5.9	-5.32	-5.65	-5.38	-5.77	-5.78	-5.05	-5.65	-5.67	-6.03	-5.33	-5.76	-5.2	-5.45	-5.38	-5.61	-5.92	-5.13	-5.55
5	-2.43	-2.98	-2.51	-2.84	-2.48	-2.45	-2.5	-2.55	-2.6	-2.51	-2.59	-2.1	-2.61	-2.43	-2.73	-1.93	-2.02	-2.36	-1.71	-2.64	-2.79	-2.33
6	-1.23	-1.36	-0.96	-0.64	-0.51	-0.57	-0.87	-0.71	-1.09	-0.75	-0.87	0.2	-0.29	-0.23	-0.23	1.54	0.58	-0.28	-0.67	-1.22	-0.23	-0.08
7	-0.9	-1.07	-0.6	-1.07	-0.12	-0.84	-0.96	-0.96	-1.21	-0.28	-0.8	0.09	-0.69	-0.37	-0.64	0.3	-0.24	-0.45	-0.64	-1.26	-0.64	-0.45
8	-0.34	-0.57	-0.22	-0.57	-0.15	-0.14	-0.4	-0.19	-0.31	-0.01	-0.29	0.03	0.03	-0.25	-0.7	-0.01	0.41	0.35	0.2	-0.1	-0.23	-0.03
9	-1.97	-1.86	-1.61	-1.19	-0.87	-1.0	-1.66	-1.16	-1.11	-1.4	-1.38	-2.99	-2.59	-1.83	-2.34	-2.27	-2.36	-2.93	-2.21	-2.16	-1.74	-2.34
10	-0.54	-0.45	-0.22	-0.18	0.52	-0.53	-0.34	-0.86	-0.27	-0.34	-0.32	0.5	0.35	0.37	0.14	0.61	-0.3	-0.23	0.07	0.98	-0.09	0.24
11	-1.13	-1.13	-0.96	-0.36	-0.8	-0.56	-0.9	-0.32	-0.11	-0.5	-0.68	-2.4	-1.45	-1.18	-0.53	-0.98	-1.81	-2.03	-1.1	-1.91	-1.57	-1.5
12	-1.12	-0.41	-0.18	-0.11	0.3	-1.07	-0.32	-0.74	-0.35	-0.6	-0.46	-1.19	-0.51	0.0	-0.45	0.37	-0.95	-1.14	-0.57	-0.2	-1.12	-0.58
13	-0.63	-0.72	-0.56	-0.03	-0.31	-0.19	-0.52	0.35	0.15	-0.3	-0.28	-4.07	-2.44	-1.73	-2.75	-2.81	-4.11	-3.97	-3.11	-2.48	-2.17	-2.96
14	-1.34	-0.18	-0.1	0.39	0.01	-0.62	-0.1	-0.11	-0.54	-0.36	-0.29	-4.08	-2.71	-1.97	-2.8	-1.85	-3.28	-2.81	-4.11	-3.68	-2.58	-2.99
15	-1.3	-0.75	-0.78	-0.82	-0.3	-0.93	-1.0	-0.66	-1.05	-0.93	-0.85	-2.14	-0.76	-1.4	-3.22	-2.4	-2.1	-2.55	-3.48	-1.59	-2.1	-2.17
Uncertainties																						
1	0.72	0.71	0.69	0.69	0.7	0.74	0.71	0.73	0.72	0.68	0.71	0.71	0.7	0.68	0.69	0.69	0.73	0.7	0.72	0.7	0.67	0.7
2	0.69	0.67	0.66	0.66	0.66	0.68	0.66	0.68	0.67	0.63	0.67	0.68	0.67	0.65	0.65	0.65	0.67	0.65	0.66	0.66	0.62	0.66
3	0.94	0.92	0.92	0.88	0.89	0.92	0.91	0.92	0.93	0.9	0.91	0.9	0.88	0.89	0.84	0.86	0.88	0.88	0.87	0.87	0.82	0.87
4	1.21	1.19	1.17	1.17	1.14	1.19	1.17	1.19	1.19	1.14	1.18	1.19	1.17	1.15	1.15	1.11	1.17	1.14	1.17	1.17	1.12	1.15
5	1.16	1.12	1.15	1.12	1.11	1.14	1.14	1.15	1.15	1.13	1.14	1.13	1.09	1.12	1.09	1.08	1.1	1.09	1.09	1.1	1.09	1.1
6	1.09	1.04	1.08	1.0	1.01	1.02	1.01	1.01	1.03	1.0	1.03	0.94	0.95	0.98	0.93	0.93	0.91	0.85	0.84	0.85	0.76	0.89
7	0.84	0.82	0.82	0.79	0.77	0.8	0.81	0.82	0.82	0.79	0.81	0.75	0.71	0.74	0.74	0.73	0.69	0.7	0.67	0.72	0.67	0.71
8	0.64	0.64	0.66	0.64	0.61	0.63	0.63	0.64	0.64	0.62	0.63	0.55	0.56	0.58	0.5	0.43	0.46	0.44	0.46	0.48	0.44	0.49
9	1.33	1.26	1.28	1.17	1.16	1.19	1.19	1.19	1.16	1.18	1.21	1.02	0.94	0.95	0.99	0.99	0.85	0.78	0.82	0.72	0.78	0.88
10	0.73	0.71	0.73	0.67	0.62	0.68	0.68	0.73	0.7	0.68	0.69	0.66	0.65	0.68	0.64	0.58	0.64	0.62	0.69	0.64	0.62	0.64
11	0.9	0.89	0.9	0.81	0.83	0.82	0.81	0.79	0.75	0.77	0.83	0.8	0.76	0.83	0.66	0.68	0.69	0.65	0.69	0.65	0.65	0.71
12	0.61	0.58	0.57	0.53	0.5	0.58	0.57	0.64	0.59	0.56	0.57	0.52	0.52	0.54	0.5	0.45	0.54	0.51	0.57	0.54	0.5	0.52
13	0.99	0.96	0.98	0.88	0.89	0.87	0.85	0.82	0.79	0.81	0.88	0.85	0.77	0.87	0.64	0.68	0.69	0.62	0.66	0.61	0.59	0.7
14	0.69	0.63	0.61	0.55	0.55	0.61	0.58	0.65	0.63	0.61	0.61	0.36	0.37	0.45	0.39	0.43	0.41	0.38	0.42	0.4	0.37	0.4
15	0.81	0.77	0.77	0.76	0.74	0.77	0.77	0.8	0.79	0.78	0.78	0.61	0.64	0.66	0.62	0.62	0.59	0.57	0.62	0.57	0.53	0.6

Table S6. Annual prior and posterior regional flux estimates with uncertainties and 2011-2020 average values in units of g C m^{-2} yr^{-1}.

	Prior											Post										
Region	2011	2012	2013	2014	2015	2016	2017	2018	2019	2020	2011-2020	2011	2012	2013	2014	2015	2016	2017	2018	2019	2020	2011-2020
Fluxes																						
1	-182.14	-145.41	-64.38	-156.47	-119.74	-163.24	-93.59	-156.13	-116.13	-54.24	-125.15	-162.71	-131.02	-53.62	-157.9	-105.85	-124.91	-89.59	-167.14	-100.28	-54.37	-114.74
2	-130.91	-111.96	-46.07	-120.74	-73.58	-90.19	-49.66	-109.5	-100.26	-34.29	-86.72	-103.68	-88.57	-35.93	-116.07	-57.5	-48.54	-39.49	-102.82	-83.84	-32.09	-70.85
3	-168.45	-172.81	-80.17	-119.58	-100.27	-132.71	-107.32	-149.71	-149.48	-95.49	-127.6	-68.13	-110.88	-56.81	-121.42	15.05	-1.38	-98.42	-130.3	-173.9	-133.73	-87.99
4	-597.98	-619.91	-545.69	-589.82	-532.47	-565.28	-538.49	-577.46	-577.59	-504.9	-564.96	-567.21	-603.2	-533.39	-576.24	-520.06	-544.93	-538.21	-561.32	-592.48	-513.06	-555.01
5	-243.22	-297.74	-251.26	-284.14	-248.02	-245.48	-250.35	-254.82	-259.88	-251.45	-258.64	-210.11	-260.7	-242.83	-273.39	-193.3	-201.88	-235.99	-170.55	-264.43	-279.19	-233.24
6	-122.52	-135.54	-96.05	-63.67	-51.49	-57.35	-86.94	-70.84	-108.73	-74.93	-86.81	20.08	-28.92	-23.31	-22.54	153.61	57.67	-27.61	-66.81	-122.2	-22.63	-8.27
7	-89.91	-107.33	-59.56	-107.46	-11.67	-83.95	-95.91	-96.38	-121.31	-27.77	-80.12	9.18	-69.44	-37.17	-63.57	29.99	-24.25	-44.68	-63.9	-126.38	-64.28	-45.45
8	-33.56	-57.16	-22.21	-56.6	-14.71	-13.87	-40.14	-18.81	-30.74	-1.48	-28.93	3.2	2.76	-24.56	-69.55	-1.37	40.87	35.33	20.19	-9.79	-23.33	-2.63
9	-197.47	-185.82	-160.95	-118.55	-86.8	-99.91	-165.54	-116.36	-110.81	-140.38	-138.26	-298.97	-259.5	-183.32	-234.31	-227.48	-236.48	-292.85	-221.28	-216.21	-173.84	-234.42
10	-54.15	-45.37	-22.07	-18.01	52.01	-52.63	-33.81	-85.83	-26.58	-34.01	-32.04	49.64	34.54	36.67	14.1	60.62	-29.84	-22.53	7.25	98.24	-9.33	23.94
11	-113.45	-112.81	-95.83	-36.24	-79.95	-55.56	-90.47	-31.8	-10.61	-50.08	-67.68	-239.73	-145.48	-117.61	-53.25	-98.1	-181.46	-202.87	-109.52	-190.6	-156.59	-149.52
12	-112.48	-41.39	-17.69	-11.44	30.38	-106.67	-32.26	-73.62	-35.35	-60.43	-46.1	-118.52	-51.44	0.04	-44.82	37.04	-95.45	-113.69	-56.76	-19.92	-112.23	-57.58
13	-62.66	-72.1	-56.45	-3.1	-30.94	-18.83	-52.19	34.63	15.06	-30.07	-27.66	-406.75	-244.13	-173.23	-275.01	-281.37	-410.58	-397.25	-310.58	-248.1	-217.0	-296.4
14	-133.83	-18.36	-9.52	39.31	1.42	-62.18	-9.57	-11.05	-54.02	-36.1	-29.39	-407.67	-270.99	-197.02	-279.63	-185.19	-327.57	-281.27	-411.42	-367.71	-258.2	-298.67
15	-130.41	-75.27	-77.77	-82.38	-30.49	-92.8	-99.83	-66.46	-104.66	-92.9	-85.3	-213.64	-75.67	-140.21	-322.45	-240.35	-209.64	-254.53	-348.19	-158.52	-209.79	-217.3
Uncertainties																						
1	72.18	70.98	68.6	69.01	69.67	73.82	70.67	73.37	72.32	67.94	70.86	71.35	70.36	68.05	68.51	68.93	72.72	69.94	71.7	69.74	67.12	69.84
2	69.45	67.49	66.14	66.04	65.6	68.09	65.87	67.54	67.47	63.11	66.68	68.22	66.69	65.46	65.38	64.8	67.12	65.03	65.81	66.05	61.57	65.61
3	94.44	91.88	91.53	88.18	88.79	92.29	91.06	92.44	92.73	89.5	91.28	90.38	87.62	89.02	83.69	85.93	87.83	87.94	87.49	86.9	82.48	86.93
4	121.29	118.55	117.45	116.69	114.37	119.03	116.91	119.47	119.29	114.3	117.74	118.71	116.66	115.47	114.68	111.43	116.87	113.52	117.21	116.71	111.54	115.28
5	116.42	112.16	114.57	111.63	111.32	114.02	113.6	114.66	115.02	113.23	113.66	113.41	109.09	111.89	108.62	108.26	109.51	108.59	108.86	110.39	108.81	109.74
6	108.97	104.27	107.94	100.49	100.58	102.25	101.07	100.87	102.86	99.89	102.92	93.6	95.03	97.72	92.53	92.73	91.45	84.88	83.92	85.01	75.76	89.26
7	83.56	81.58	82.21	79.09	76.91	80.12	80.81	82.05	82.06	78.51	80.69	74.59	70.57	74.39	74.11	72.98	68.99	70.21	66.75	72.18	66.6	71.14
8	64.27	63.9	66.41	63.94	61.11	63.17	62.69	63.92	63.65	61.54	63.46	54.78	56.15	58.29	49.81	42.79	45.83	44.13	45.72	47.66	44.04	48.92
9	132.94	126.27	127.53	117.38	116.02	118.87	118.52	119.43	115.96	117.63	121.06	101.68	93.7	94.79	99.11	98.75	85.24	77.58	81.73	72.2	78.12	88.29
10	73.15	70.92	72.87	67.38	62.09	67.72	68.05	72.87	69.58	67.79	69.24	65.68	64.83	67.91	64.3	57.73	63.79	62.15	68.62	64.36	61.72	64.11
11	90.4	89.0	89.99	80.75	83.42	82.26	80.71	79.21	75.32	76.59	82.77	80.45	76.31	83.48	66.0	67.84	68.62	65.23	69.47	65.05	65.3	70.77
12	61.5	58.46	57.28	53.15	49.52	58.16	56.84	63.81	59.04	56.15	57.39	51.76	51.76	53.66	49.98	45.43	54.28	50.55	57.25	54.19	49.76	51.86
13	99.31	96.26	97.56	87.83	89.04	87.25	84.93	81.51	78.77	80.8	88.33	84.58	76.81	87.1	63.83	67.7	68.85	62.2	66.3	60.94	59.33	69.76
14	68.87	62.84	60.88	55.13	54.74	60.91	57.95	64.57	63.23	61.0	61.01	36.44	36.99	45.34	38.7	43.17	40.84	38.19	41.64	40.32	36.79	39.84
15	81.18	77.25	77.26	76.25	73.85	76.88	77.02	79.9	79.28	77.91	77.68	60.64	63.69	66.49	62.37	61.57	59.18	56.63	61.98	56.65	52.88	60.21

Table S7. Annual prior and posterior regional flux estimates with uncertainties and 2011-2020 average values in units of kg CO_2 m^{-2} yr^{-1}.

	Prior											Post										
Region	2011	2012	2013	2014	2015	2016	2017	2018	2019	2020	2011-2020	2011	2012	2013	2014	2015	2016	2017	2018	2019	2020	2011-2020
Fluxes																						
1	-0.67	-0.53	-0.24	-0.57	-0.44	-0.6	-0.34	-0.57	-0.43	-0.2	-0.46	-0.6	-0.48	-0.2	-0.58	-0.39	-0.46	-0.33	-0.61	-0.37	-0.2	-0.42
2	-0.48	-0.41	-0.17	-0.44	-0.27	-0.33	-0.18	-0.4	-0.37	-0.13	-0.32	-0.38	-0.32	-0.13	-0.43	-0.21	-0.18	-0.14	-0.38	-0.31	-0.12	-0.26
3	-0.62	-0.63	-0.29	-0.44	-0.37	-0.49	-0.39	-0.55	-0.55	-0.35	-0.47	-0.25	-0.41	-0.21	-0.45	0.06	-0.01	-0.36	-0.48	-0.64	-0.49	-0.32
4	-2.19	-2.27	-2.0	-2.16	-1.95	-2.07	-1.97	-2.12	-2.12	-1.85	-2.07	-2.08	-2.21	-1.96	-2.11	-1.91	-2.0	-1.97	-2.06	-2.17	-1.88	-2.04
5	-0.89	-1.09	-0.92	-1.04	-0.91	-0.9	-0.92	-0.93	-0.95	-0.92	-0.95	-0.77	-0.96	-0.89	-1.0	-0.71	-0.74	-0.87	-0.63	-0.97	-1.02	-0.86
6	-0.45	-0.5	-0.35	-0.23	-0.19	-0.21	-0.32	-0.26	-0.4	-0.27	-0.32	0.07	-0.11	-0.09	-0.08	0.56	0.21	-0.1	-0.24	-0.45	-0.08	-0.03
7	-0.33	-0.39	-0.22	-0.39	-0.04	-0.31	-0.35	-0.35	-0.44	-0.1	-0.29	0.03	-0.25	-0.14	-0.23	0.11	-0.09	-0.16	-0.23	-0.46	-0.24	-0.17
8	-0.12	-0.21	-0.08	-0.21	-0.05	-0.05	-0.15	-0.07	-0.11	-0.01	-0.11	0.01	0.01	-0.09	-0.26	-0.01	0.15	0.13	0.07	-0.04	-0.09	-0.01
9	-0.72	-0.68	-0.59	-0.43	-0.32	-0.37	-0.61	-0.43	-0.41	-0.51	-0.51	-1.1	-0.95	-0.67	-0.86	-0.83	-0.87	-1.07	-0.81	-0.79	-0.64	-0.86
10	-0.2	-0.17	-0.08	-0.07	0.19	-0.19	-0.12	-0.31	-0.1	-0.12	-0.12	0.18	0.13	0.13	0.05	0.22	-0.11	-0.08	0.03	0.36	-0.03	0.09
11	-0.42	-0.41	-0.35	-0.13	-0.29	-0.2	-0.33	-0.12	-0.04	-0.18	-0.25	-0.88	-0.53	-0.43	-0.2	-0.36	-0.67	-0.74	-0.4	-0.7	-0.57	-0.55
12	-0.41	-0.15	-0.06	-0.04	0.11	-0.39	-0.12	-0.27	-0.13	-0.22	-0.17	-0.43	-0.19	0.0	-0.16	0.14	-0.35	-0.42	-0.21	-0.07	-0.41	-0.21
13	-0.23	-0.26	-0.21	-0.01	-0.11	-0.07	-0.19	0.13	0.06	-0.11	-0.1	-1.49	-0.9	-0.64	-1.01	-1.03	-1.51	-1.46	-1.14	-0.91	-0.8	-1.09
14	-0.49	-0.07	-0.03	0.14	0.01	-0.23	-0.04	-0.04	-0.2	-0.13	-0.11	-1.49	-0.99	-0.72	-1.03	-0.68	-1.2	-1.03	-1.51	-1.35	-0.95	-1.1
15	-0.48	-0.28	-0.29	-0.3	-0.11	-0.34	-0.37	-0.24	-0.38	-0.34	-0.31	-0.78	-0.28	-0.51	-1.18	-0.88	-0.77	-0.93	-1.28	-0.58	-0.77	-0.8
Uncertainties																						
1	0.26	0.26	0.25	0.25	0.26	0.27	0.26	0.27	0.27	0.25	0.26	0.26	0.26	0.25	0.25	0.25	0.27	0.26	0.26	0.26	0.25	0.26
2	0.25	0.25	0.24	0.24	0.24	0.25	0.24	0.25	0.25	0.23	0.24	0.25	0.24	0.24	0.24	0.24	0.25	0.24	0.24	0.24	0.23	0.24
3	0.35	0.34	0.34	0.32	0.33	0.34	0.33	0.34	0.34	0.33	0.33	0.33	0.32	0.33	0.31	0.32	0.32	0.32	0.32	0.32	0.3	0.32
4	0.44	0.43	0.43	0.43	0.42	0.44	0.43	0.44	0.44	0.42	0.43	0.44	0.43	0.42	0.42	0.41	0.43	0.42	0.43	0.43	0.41	0.42
5	0.43	0.41	0.42	0.41	0.41	0.42	0.42	0.42	0.42	0.42	0.42	0.42	0.4	0.41	0.4	0.4	0.4	0.4	0.4	0.4	0.4	0.4
6	0.4	0.38	0.4	0.37	0.37	0.37	0.37	0.37	0.38	0.37	0.38	0.34	0.35	0.36	0.34	0.34	0.34	0.31	0.31	0.31	0.28	0.33
7	0.31	0.3	0.3	0.29	0.28	0.29	0.3	0.3	0.3	0.29	0.3	0.27	0.26	0.27	0.27	0.27	0.25	0.26	0.24	0.26	0.24	0.26
8	0.24	0.23	0.24	0.23	0.22	0.23	0.23	0.23	0.23	0.23	0.23	0.2	0.21	0.21	0.18	0.16	0.17	0.16	0.17	0.17	0.16	0.18
9	0.49	0.46	0.47	0.43	0.43	0.44	0.43	0.44	0.43	0.43	0.44	0.37	0.34	0.35	0.36	0.36	0.31	0.28	0.3	0.26	0.29	0.32
10	0.27	0.26	0.27	0.25	0.23	0.25	0.25	0.27	0.26	0.25	0.25	0.24	0.24	0.25	0.24	0.21	0.23	0.23	0.25	0.24	0.23	0.24
11	0.33	0.33	0.33	0.3	0.31	0.3	0.3	0.29	0.28	0.28	0.3	0.29	0.28	0.31	0.24	0.25	0.25	0.24	0.25	0.24	0.24	0.26
12	0.23	0.21	0.21	0.19	0.18	0.21	0.21	0.23	0.22	0.21	0.21	0.19	0.19	0.2	0.18	0.17	0.2	0.19	0.21	0.2	0.18	0.19
13	0.36	0.35	0.36	0.32	0.33	0.32	0.31	0.3	0.29	0.3	0.32	0.31	0.28	0.32	0.23	0.25	0.25	0.23	0.24	0.22	0.22	0.26
14	0.25	0.23	0.22	0.2	0.2	0.22	0.21	0.24	0.23	0.22	0.22	0.13	0.14	0.17	0.14	0.16	0.15	0.14	0.15	0.15	0.13	0.15
15	0.3	0.28	0.28	0.28	0.27	0.28	0.28	0.29	0.29	0.29	0.28	0.22	0.23	0.24	0.23	0.23	0.22	0.21	0.23	0.21	0.19	0.22

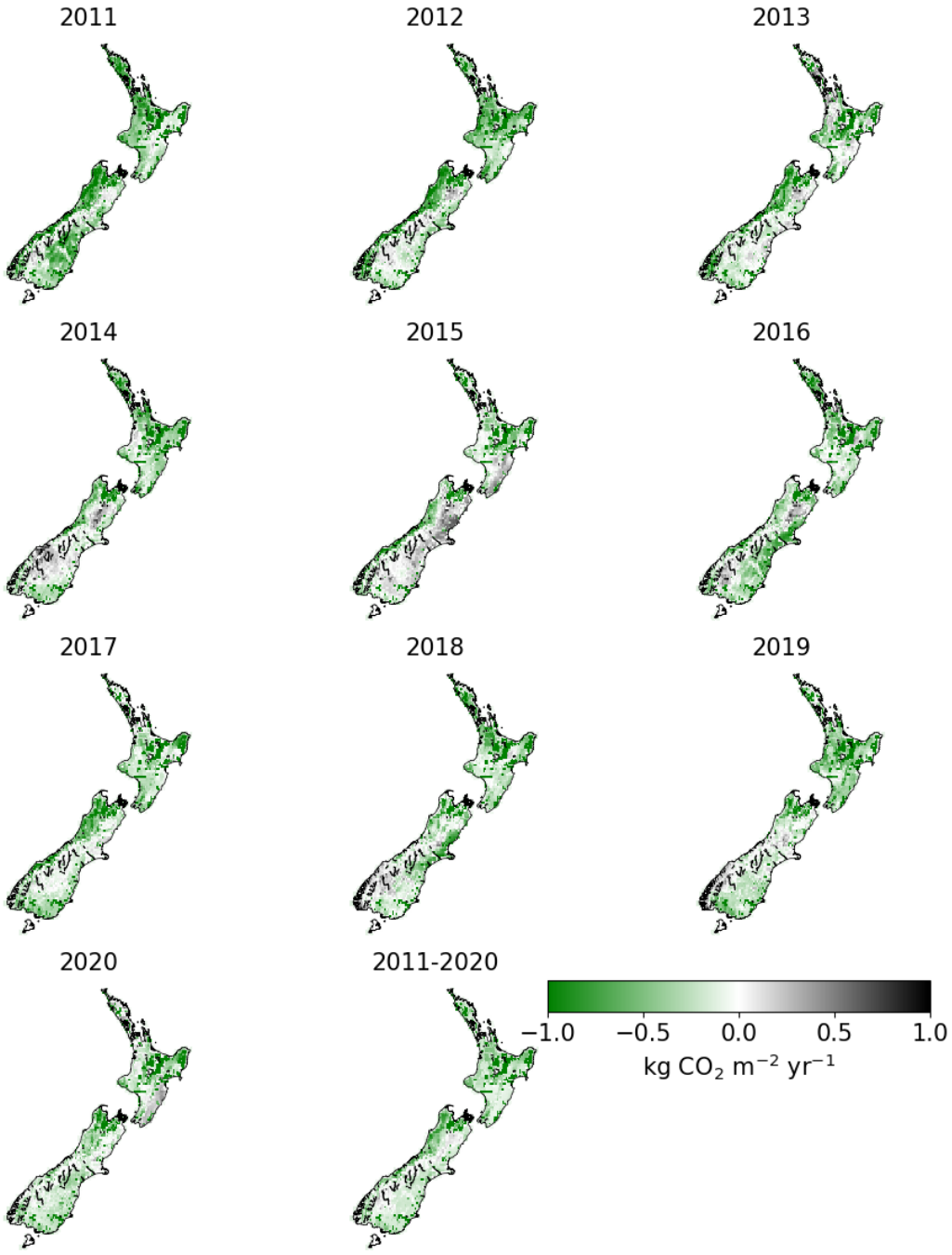

Figure S9. Spatial distribution of the prior fluxes averaged for each year between 2011 and 2020.

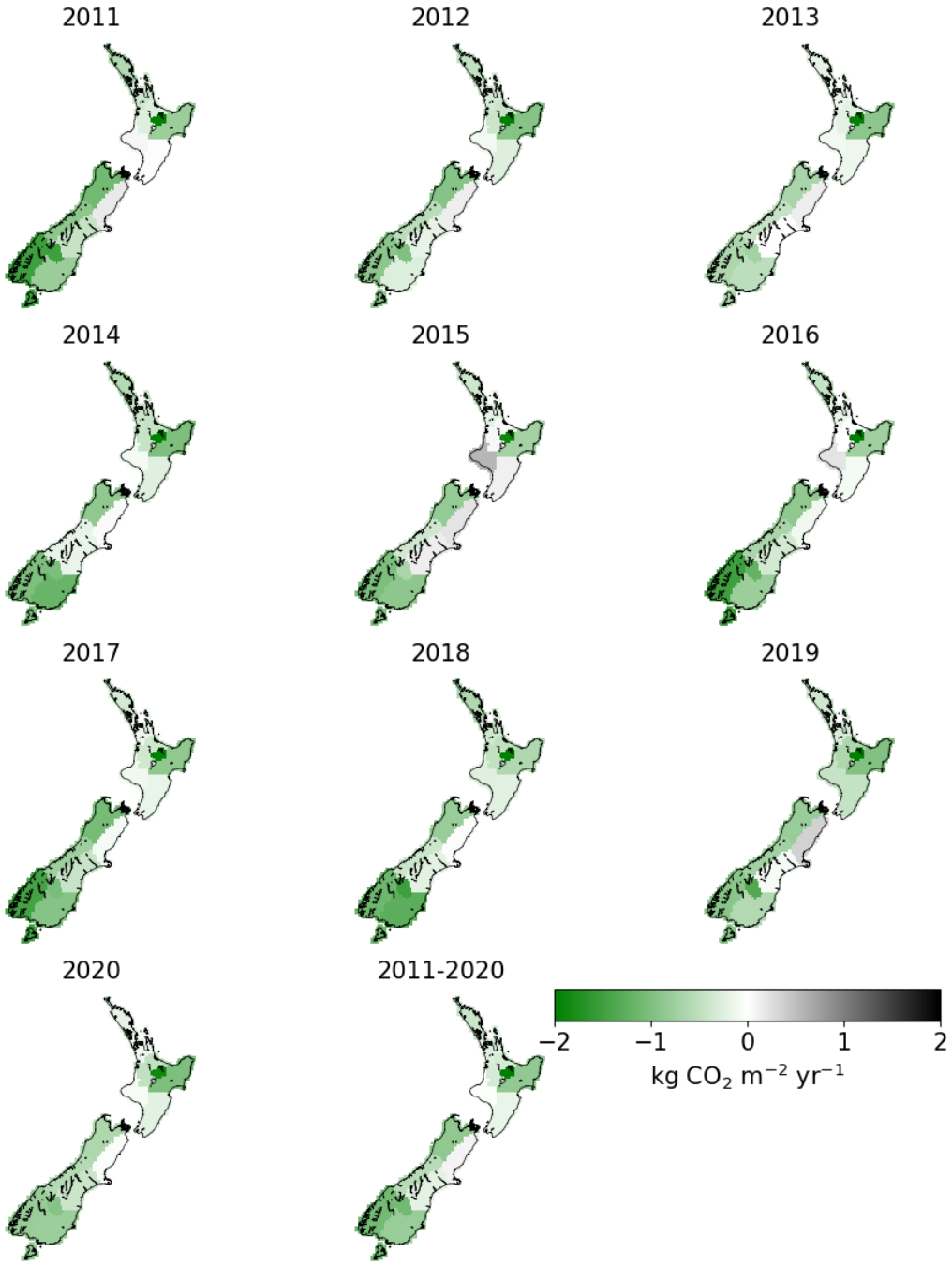

Figure S10. Regional posterior fluxes averaged for each year between 2011 and 2020.

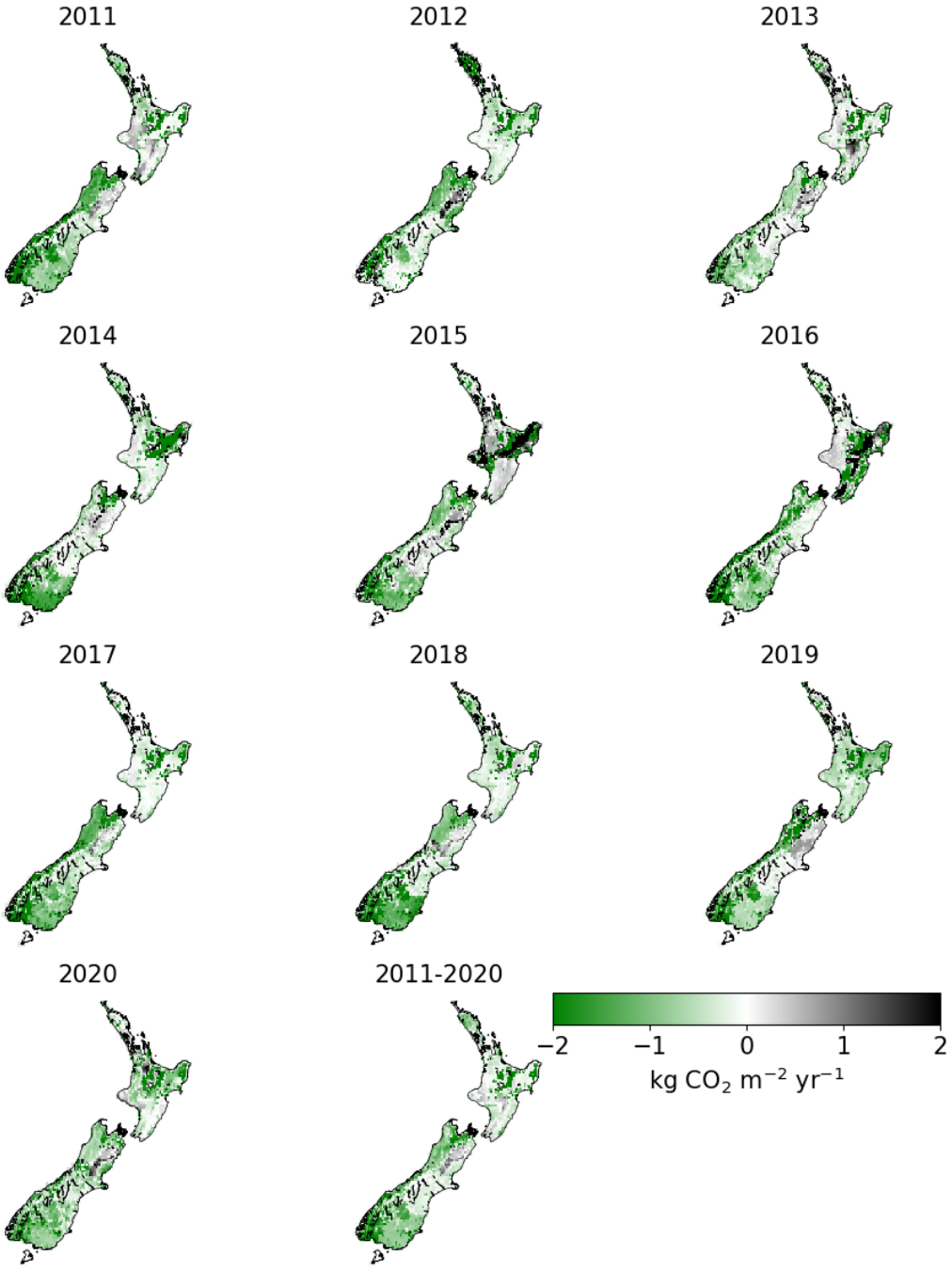

Figure S11. Spatial distribution of the posterior fluxes by scaling the prior flux maps with the regional posterior estimates and averaged for each year between 2011 and 2020.

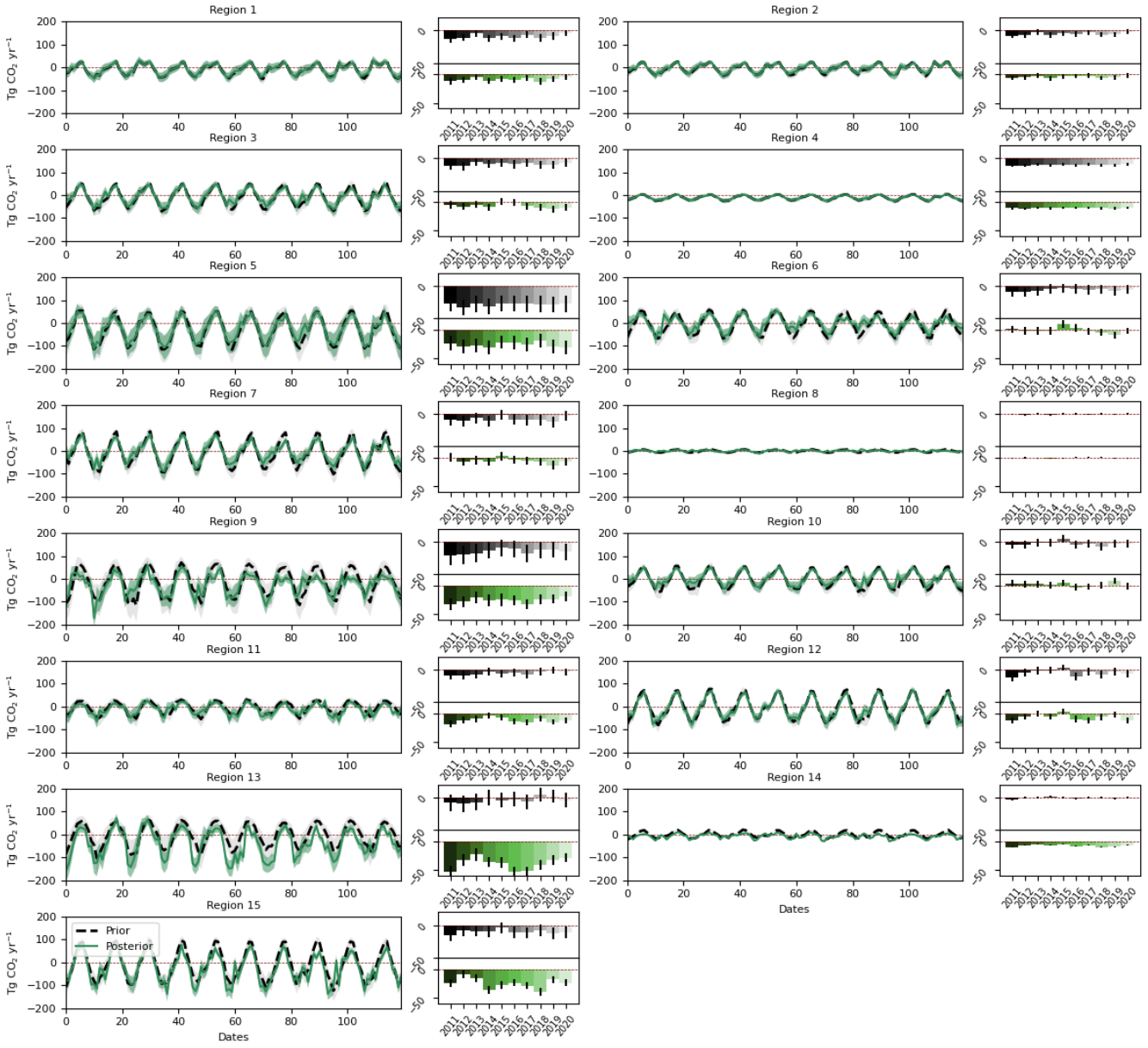

Figure S12. Monthly (left) and annual (right) CO_2 prior (black) and posterior (green) net air-land flux estimates for all land inversion regions.

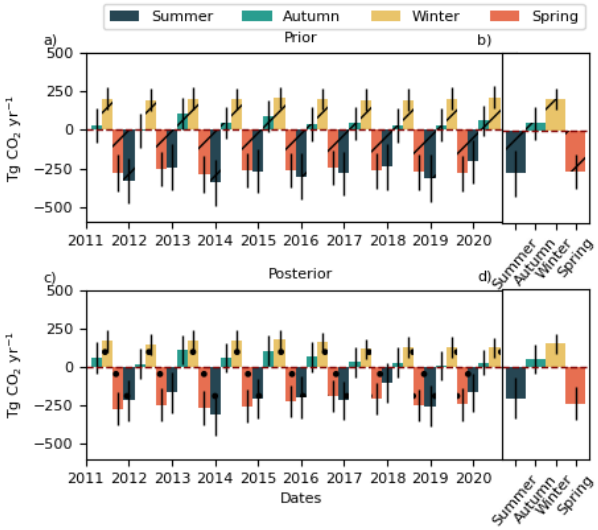

Figure S13. Mean North-Island annual seasonal (summer – December to February, autumn – March to May, winter – June to August, spring – September to November) CO_2 prior (a) and posterior (c) net air-land flux estimates. Subplots b) and d) show the 2011-2020 average values for each season. The first and last season is removed from the plot and calculation due to insufficient number of months to calculate the seasonal average.

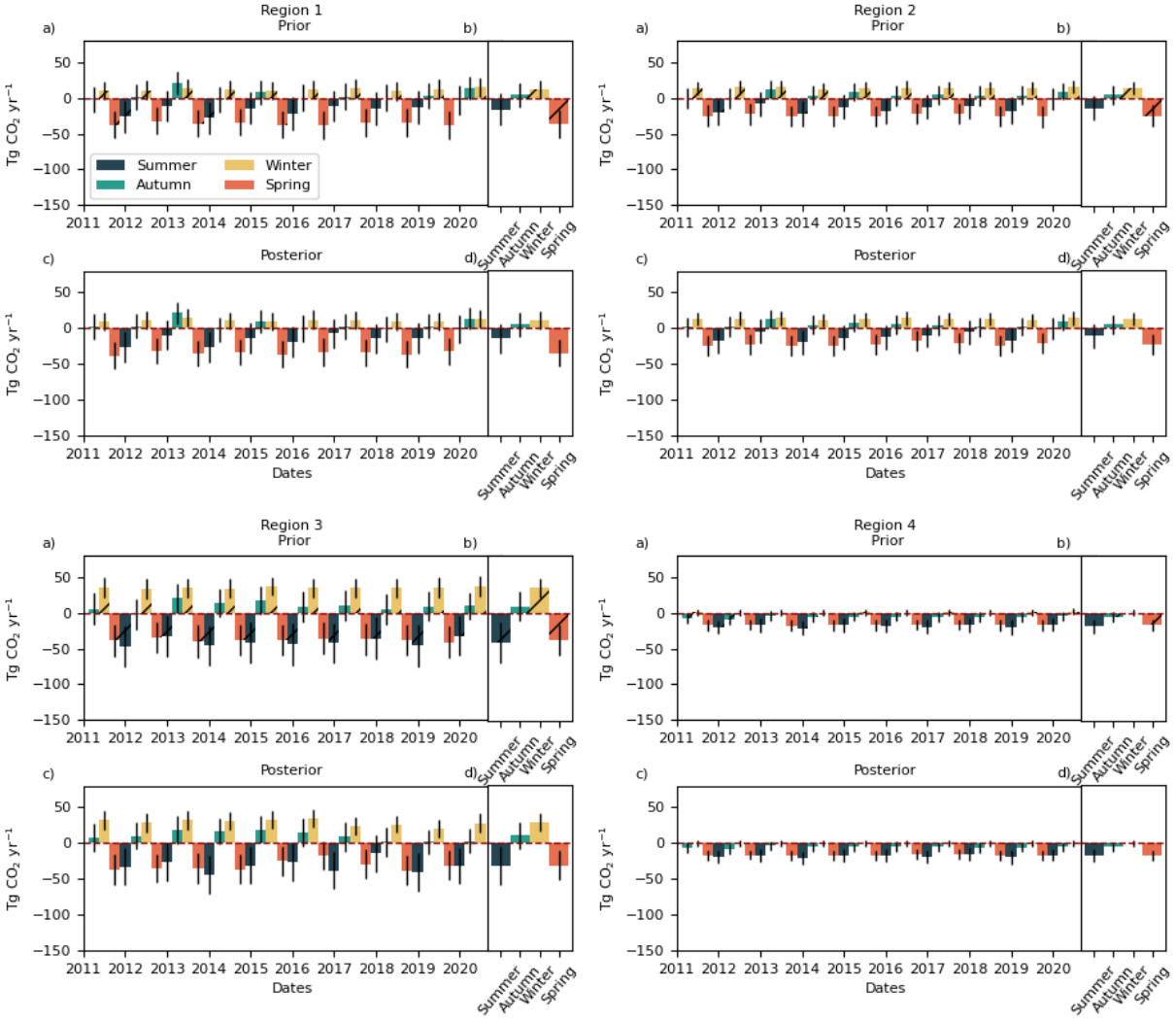

Figure S14. Mean annual seasonal (summer – December to February, autumn – March to May, winter – June to August, spring – September to November) CO_2 prior (a) and posterior (c) net air-land flux estimates for the land regions. Subplots b) and d) show the 2011-2020 average values for each season. The first and last season is removed from the plot and calculation due to insufficient number of months to calculate the seasonal average.

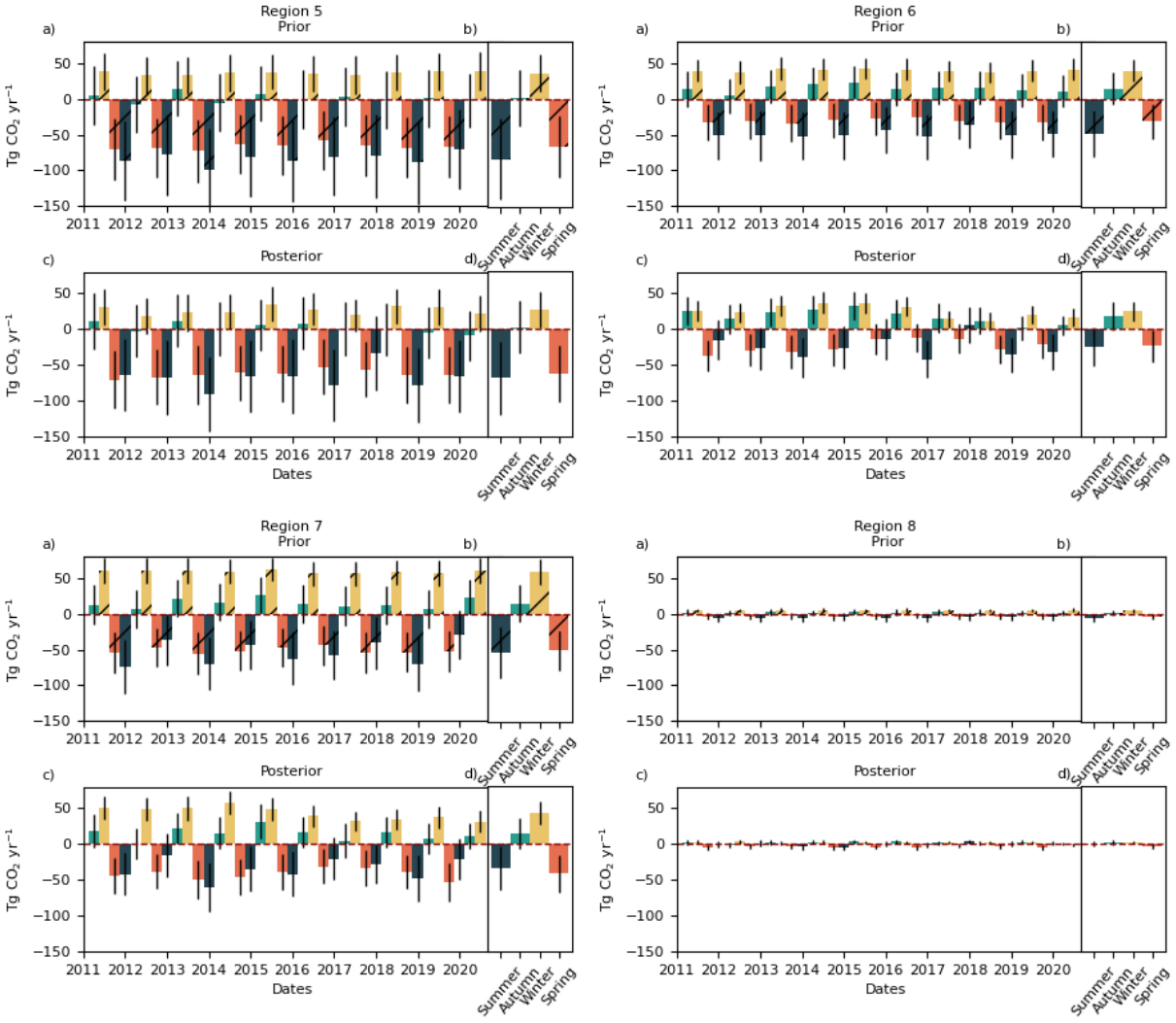

Figure S14. Continued.

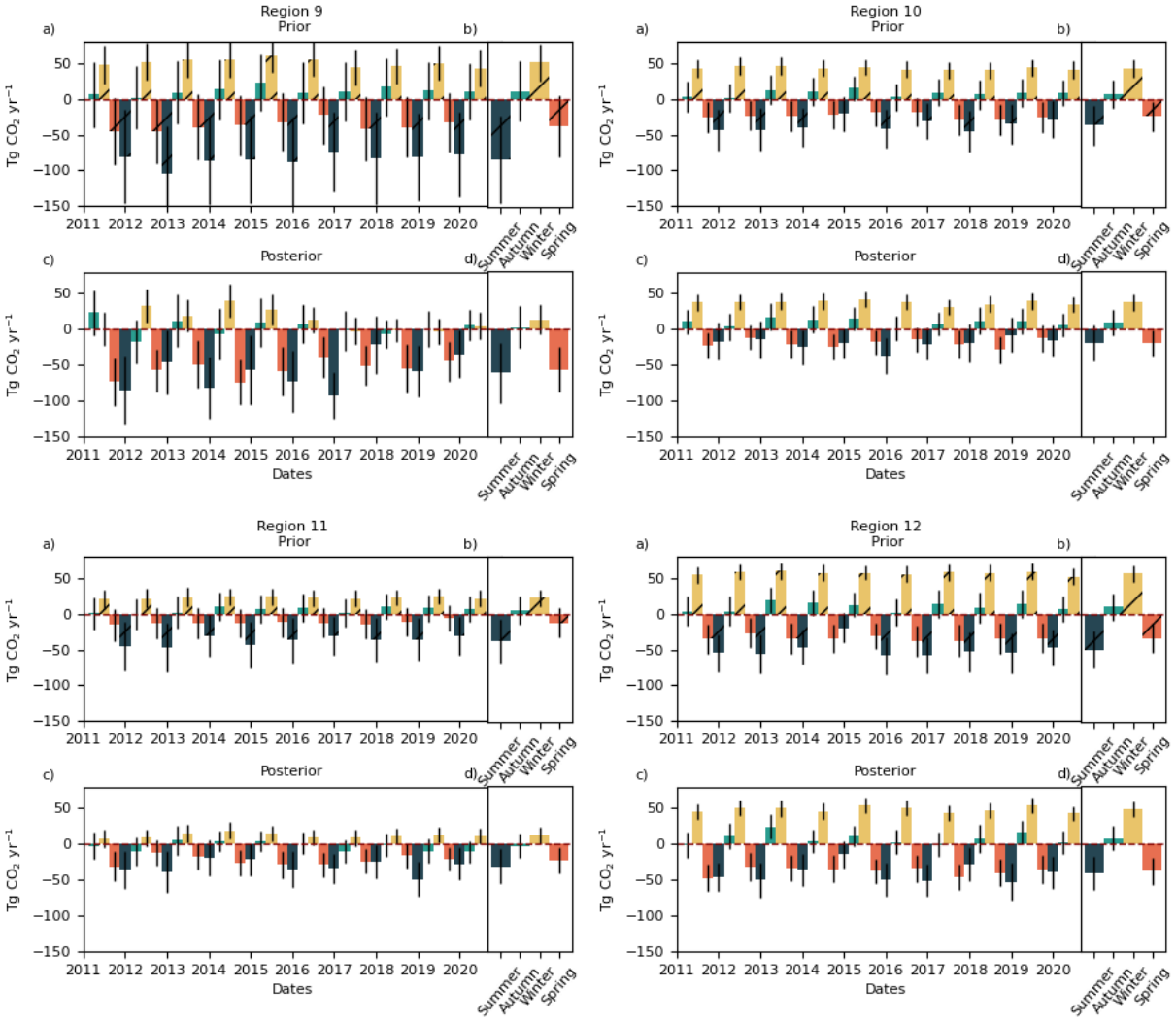

Figure S14. Continued.

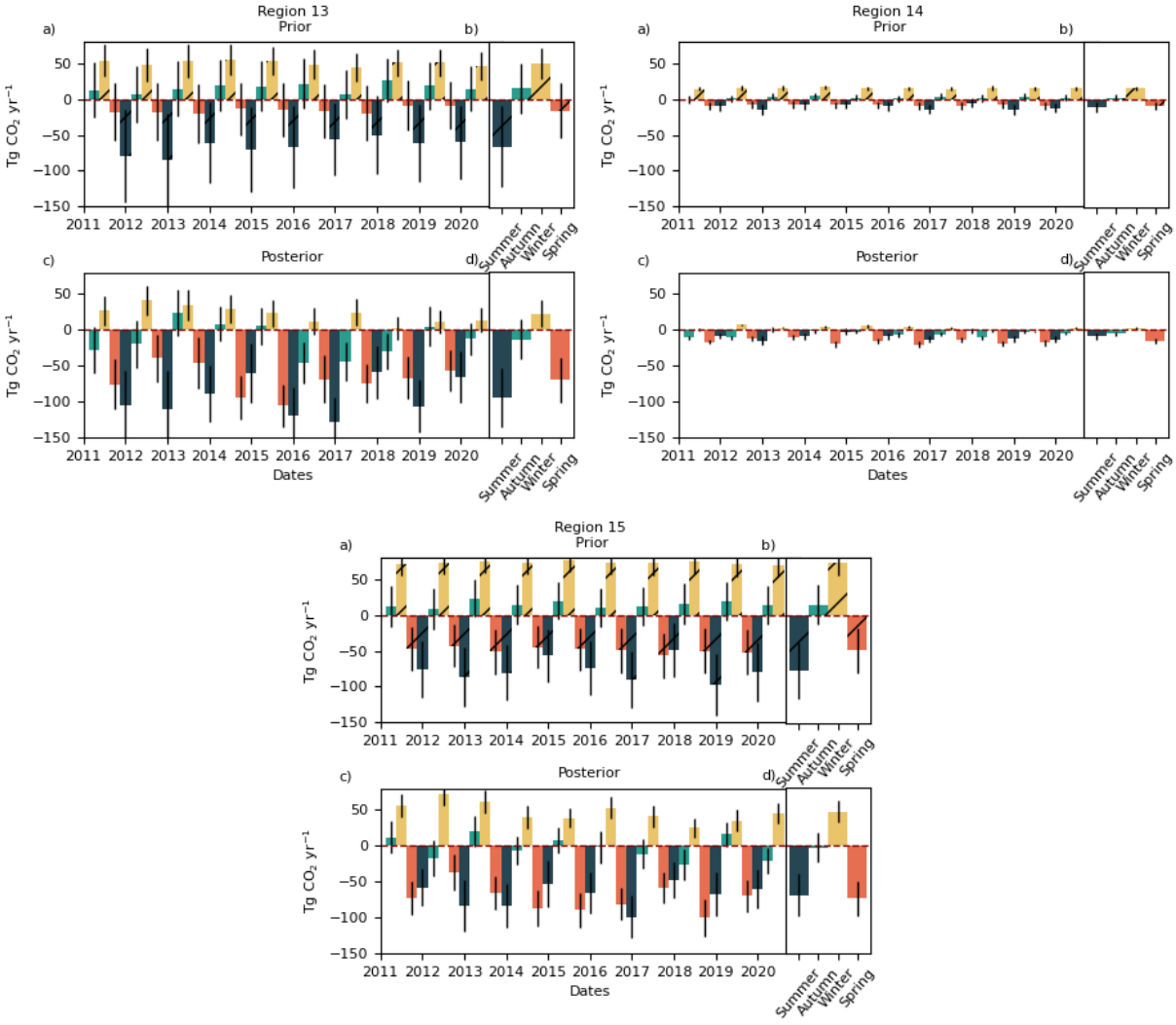

Figure S14. Continued.

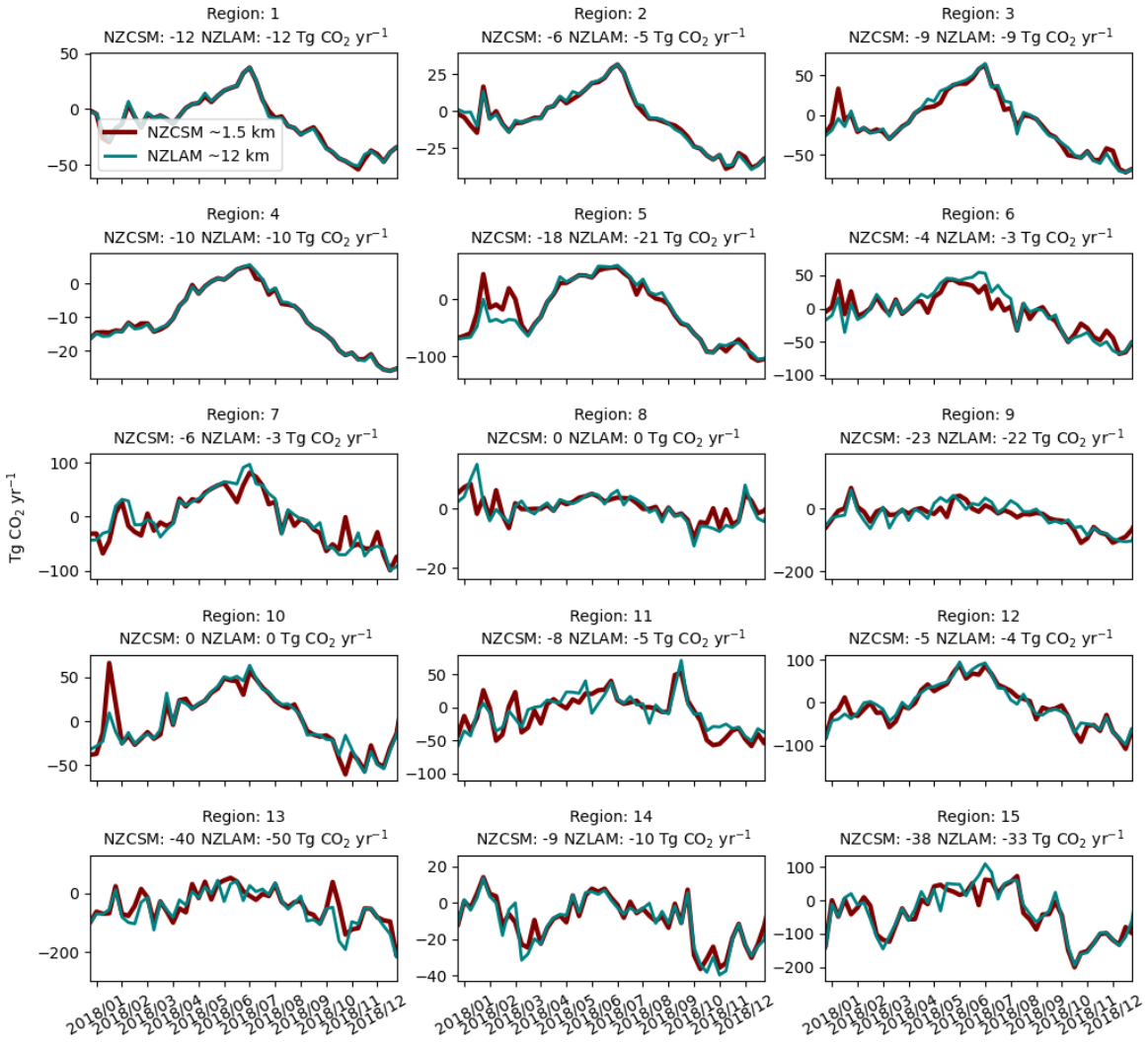

Figure S15. Time-series of the transport model sensitivity test for each inversion region.

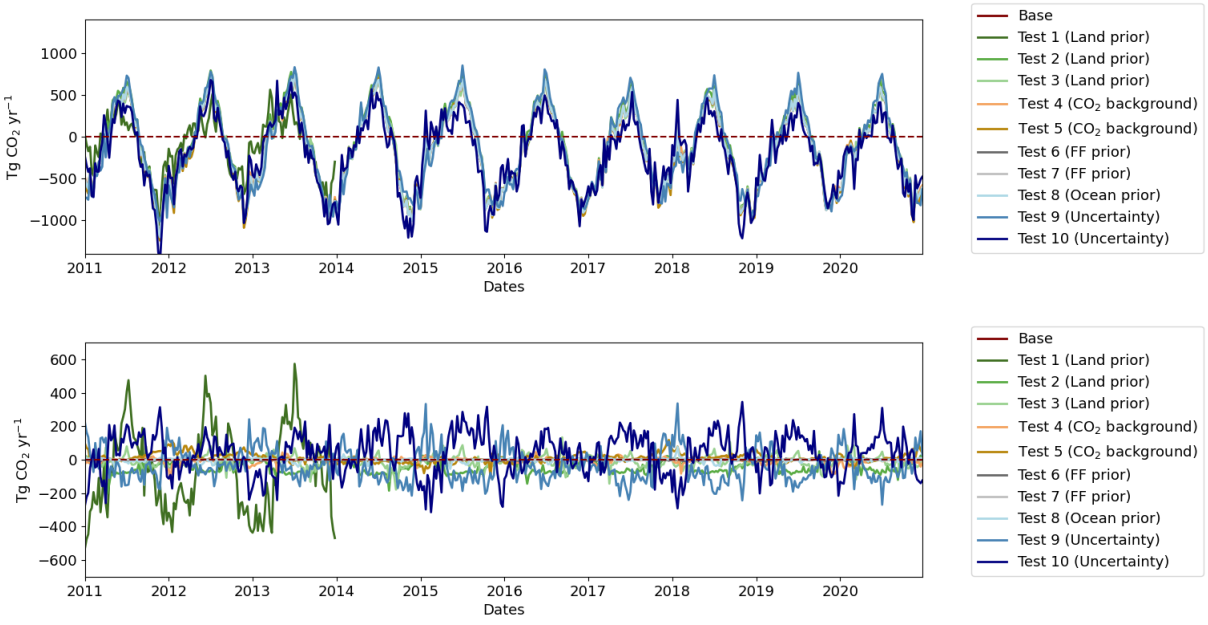

Figure S16. Time-series of the sensitivity tests for New Zealand (top plot) and difference relative to the base inversion results (bottom plot). A detailed description of the setup in each test can be found in Tabel 3.

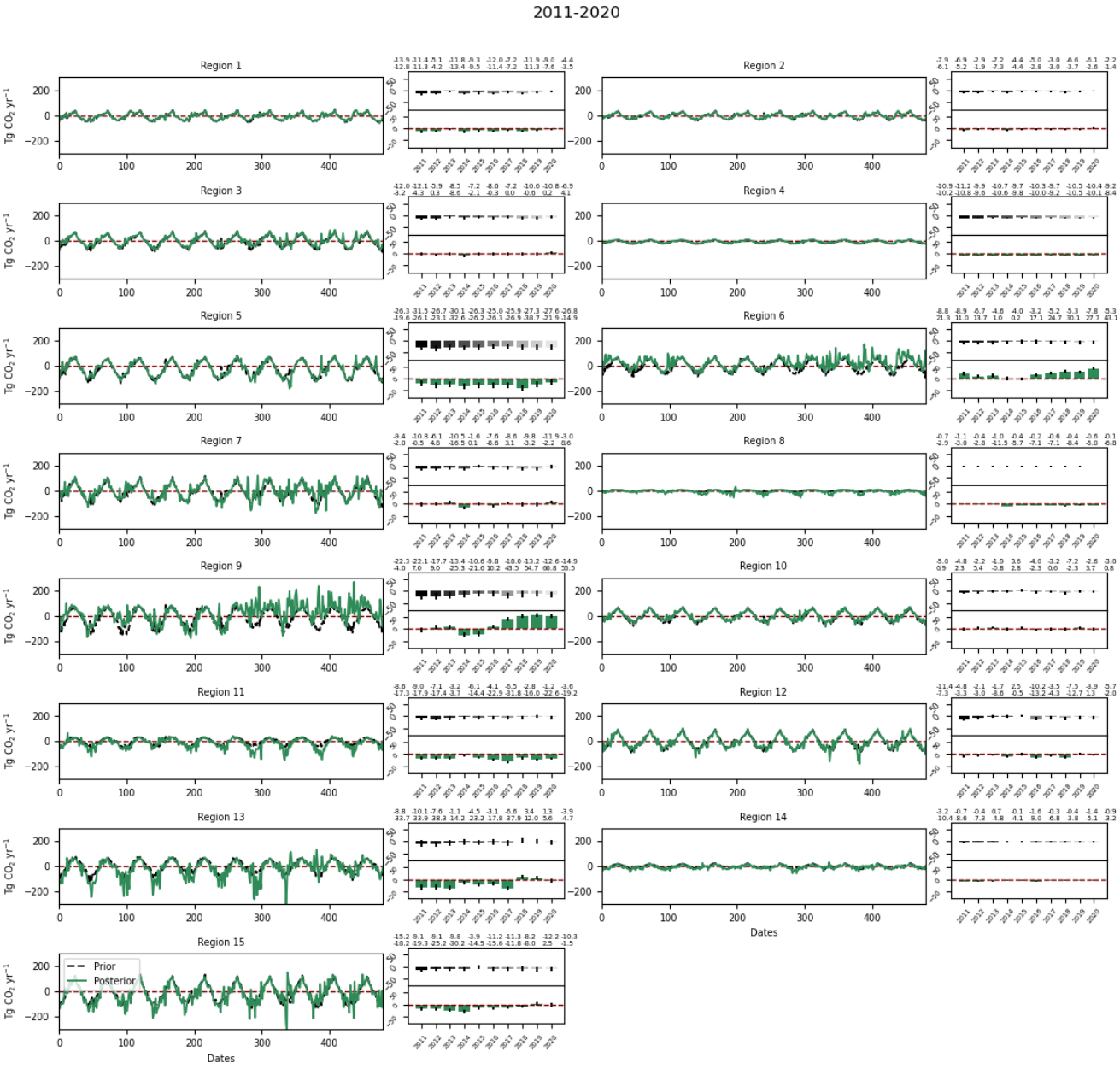

Figure S17. Diurnal cycle test results for the land inversion regions.

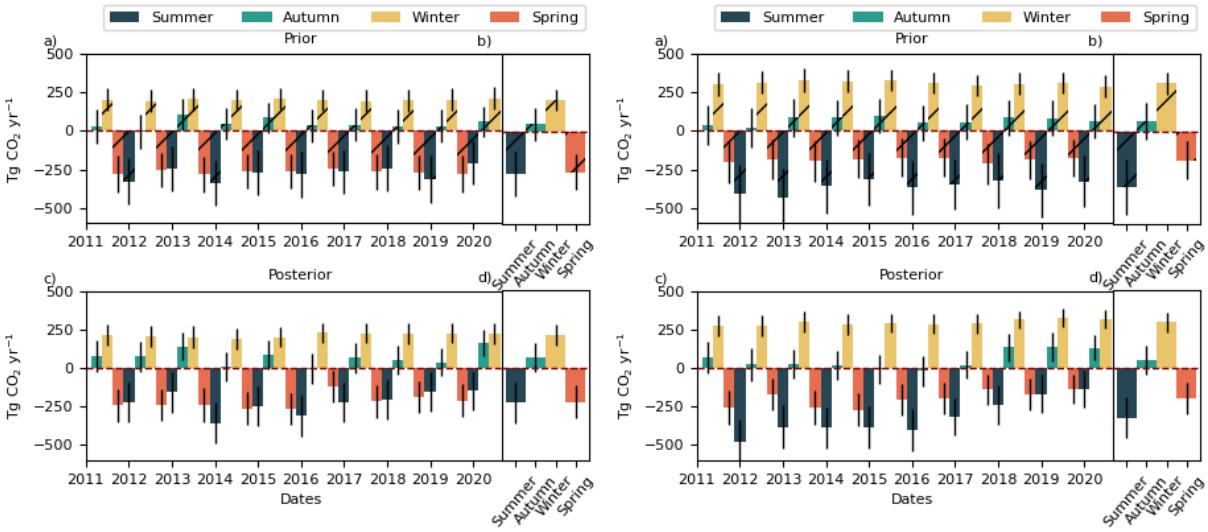

Figure S18. Mean annual seasonal (summer – December to February, autumn – March to May, winter – June to August, spring – September to November) CO_2 prior (a) and posterior (c) net air-land flux estimates for the North (left) and South Island (right) from the diurnal cycle test. Subplots b) and d) show the 2011-2020 average values for each season. The first and last season is removed from the plot and calculation due to insufficient number of months to calculate the seasonal average.

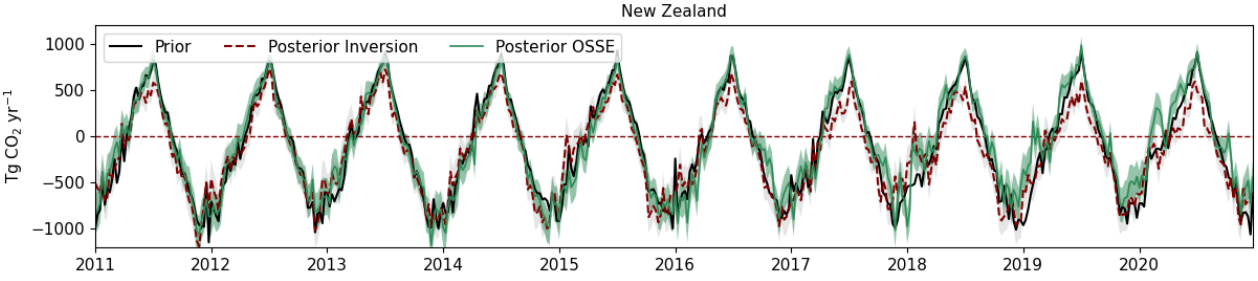

Figure S19. Timseries of the prior fluxes (black), diurnal cycle (green) and base inversion (red) posterior fluxes.

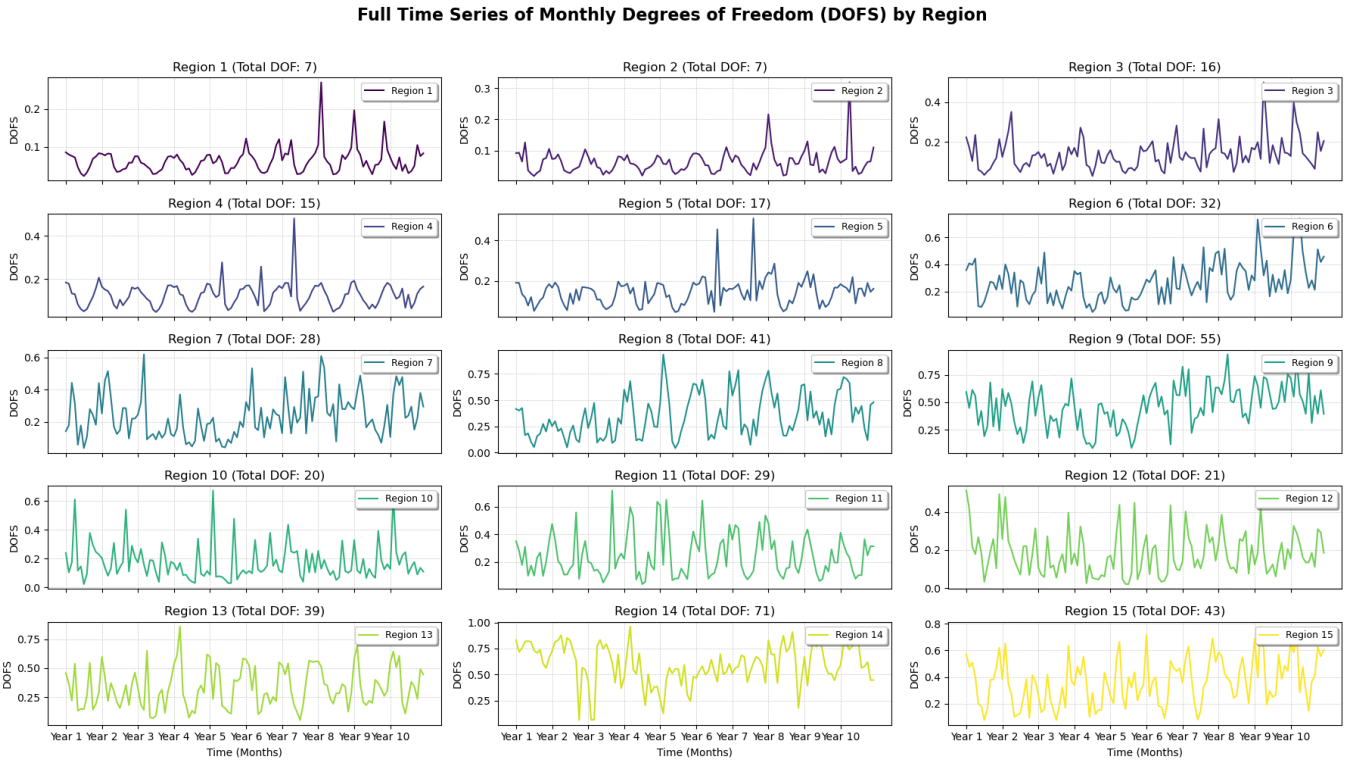

Figure S20. Timeseries of Monthly mean Degrees of Freedom (DOFs) for each inversion region.

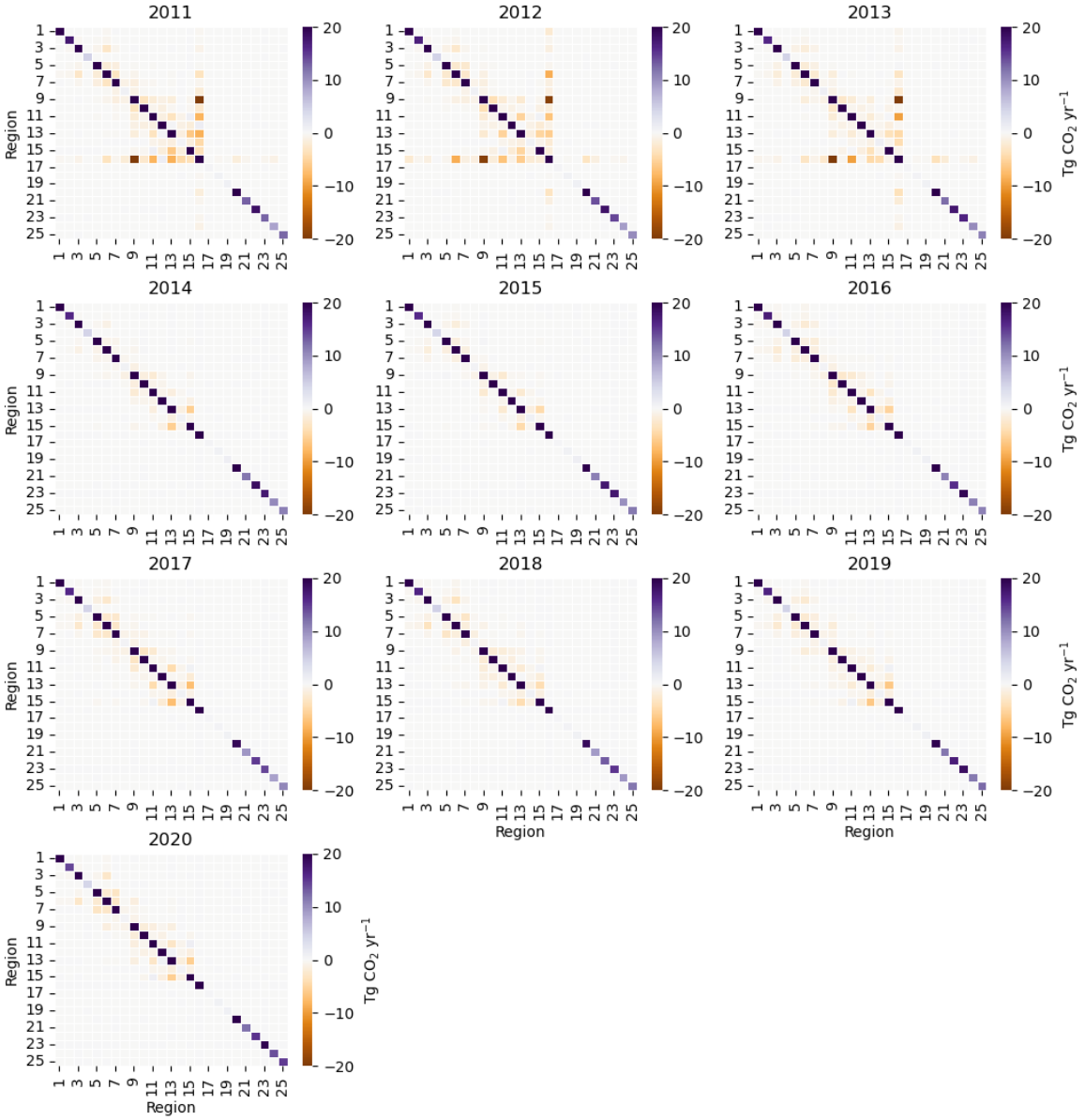

Figure S21. Posterior annual covariance matrix for individual years in 2011-2020.

References

Berhe, A. A., Barnes, R. T., Six, J., and Marín-Spiotta, E.: Role of soil erosion in biogeochemical cycling of essential elements: carbon, nitrogen, and phosphorus, Annual Review of Earth and Planetary Sciences, 46, 521–548, 2018.

Bianchi, T. S., Arndt, S., Austin, W. E., Benn, D. I., Bertrand, S., Cui, X., Faust, J. C., Koziorowska-Makuch, K., Moy, C. M., Savage, C., et al.: Fjords as aquatic critical zones (ACZs), Earth-Science Reviews, 203, 103 145, 2020.

Brailsford, G. W., Stephens, B. B., Gomez, A. J., Riedel, K., Mikaloff Fletcher, S. E., Nichol, S. E., and Manning, M. R.: Long-term continuous atmospheric CO_2 measurements at Baring Head, New Zealand, Atmospheric Measurement Techniques, 5, 3109–3117, https://doi.org/10.5194/amt-5-3109-2012, 2012.

Bush, M., Allen, T., Bain, C., Boutle, I., Edwards, J., Finnenkoetter, A., Franklin, C., Hanley, K., Lean, H., Lock, A., Manners, J., Mittermaier, M., Morcrette, C., North, R., Petch, J., Short, C., Vosper, S., Walters, D., Webster, S., Weeks, M., Wilkinson, J., Wood, N., and Zerroukat, M.: The first Met Office Unified Model–JULES Regional Atmosphere and Land configuration, RAL1, Geoscientific Model Development, 13, 1999–2029, https://doi.org/10.5194/gmd-13-1999-2020, 2020.

CARS: CSIRO Atlas of Regional Seas, Salinity at standard depths, version: 2009.A.1.1, www.marine.csiro.au/atlas/, accessed on 19-07-2021, 2009.

Cleveland, R. B., Cleveland, W. S., McRae, J. E., and Terpenning, I.: STL: A seasonal-trend decomposition, Journal of Official Statistics, 6, 3–73, 1990.

Davies, T., Cullen, M. J., Malcolm, A. J., Mawson, M., Staniforth, A., White, A., and Wood, N.: A new dynamical core for the Met Office's global and regional modelling of the atmosphere, Quarterly Journal of the Royal Meteorological Society: A journal of the atmospheric sciences, applied meteorology and physical oceanography, 131, 1759–1782, 2005.

Dickson, A. G., Sabine, C. L., and Christian, J. R., eds.: Guide to Best Practices for Ocean CO_2 Measurements, PICES Special Publication 3, 191 pp, 2007.

Doherty, J.: Calibration and uncertainty analysis for complex environmental models, Watermark Numerical Computing Brisbane, Australia, 2015.

Dymond, J. R.: Soil erosion in New Zealand is a net sink of CO2, Earth Surface Processes and Landforms, 35, 1763–1772, 2010.

Enting, I. G.: Inverse problems in atmospheric constituent transport, Cambridge University Press, 2002.

Gurney, K. R., Law, R. M., Denning, A. S., Rayner, P. J., Pak, B. C., Baker, D., Bousquet, P., Bruhwiler, L., Chen, Y.-H., Ciais, P., et al.: Transcom 3 inversion intercomparison: Model mean results for the estimation of seasonal carbon sources and sinks, Global Biogeochemical Cycles, 18, 2004.

Hall, B. D., Crotwell, A. M., Kitzis, D. R., Mefford, T., Miller, B. R., Schibig, M. F., and Tans, P. P.: Revision of the World Meteorological Organization Global Atmosphere Watch (WMO/GAW) CO_2 calibration scale, Atmospheric Measurement Techniques, 14, 3015–3032, https://doi.org/10.5194/amt-14-3015-2021, 2021.

Hall, G. M.: Mitigating an organization's future net carbon emissions by native forest restoration, Ecological Applications, 11, 1622–1633, 2001.

Hersbach, H., Bell, B., Berrisford, P., Biavati, G., Horányi, A., Muñoz Sabater, J., Nicolas, J., Peubey, C., Radu, R., Rozum, I., Schepers, D., Simmons, A., Soci, C., Dee, D., and Thépaut, J.-N.: ERA5 hourly data on single levels from 1979 to present, https://doi.org/10.24381/cds.adbb2d47, accessed on 14-07-2021, 2018.

Hersbach, H., Bell, B., Berrisford, P., Biavati, G., Horányi, A., Muñoz Sabater, J., Nicolas, J., Peubey, C., Radu, R., Rozum, I., Schepers, D., Simmons, A., Soci, C., Dee, D., and Thépaut, J.-N.: ERA5 monthly averaged data on single levels from 1979 to present, https://doi.org/10.24381/cds.f17050d7, accessed on 14-07-2021, 2019.

Hovius, N., Stark, C. P., and Allen, P. A.: Sediment flux from a mountain belt derived by landslide mapping, Geology, 25, 231–234, 1997.

Kountouris, P., Gerbig, C., Rödenbeck, C., Karstens, U., Koch, T. F., and Heimann, M.: Atmospheric CO_2 inversions on the mesoscale using data-driven prior uncertainties: methodology and system evaluation, Atmospheric Chemistry and Physics, 18, 3027–3045, 2018.

Landcare Research: LCDB v5.0 - Land Cover Database version 5.0, Mainland, New Zealand (5.0) [dataset], https://doi.org/10.26060/W5B4-WK93, 2020.

Landschützer, P., Gruber, N., and Bakker, D. C. E.: Decadal variations and trends of the global ocean carbon sink, Global Biogeochemical Cycles, 30, 1396–1417, https://doi.org/https://doi.org/10.1002/2015GB005359, 2016.

Landschützer, P., Gruber, N., and Bakker, D. C. E.: An observation-based global monthly gridded sea surface pCO_2 product from 1982 onward and its monthly climatology (NCEI Accession 0160558). Version 5.5. NOAA National Centers for Environmental Information, https://doi.org/https://doi.org/10.7289/V5Z899N6, 2020a.

Landschützer, P., Laruelle, G. G., Roobaert, A., and Regnier, P.: A uniform pCO_2 climatology combining open and coastal oceans, Earth System Science Data, 12, 2537–2553, https://doi.org/10.5194/essd-12-2537-2020, 2020b.

Lauerwald, R., Allen, G. H., Deemer, B. R., Liu, S., Maavara, T., Raymond, P., Alcott, L., Bastviken, D., Hastie, A., Holgerson, M. A., et al.: Inland water greenhouse gas budgets for RECCAP2: 2. Regionalization and homogenization of estimates, Global Biogeochemical Cycles, 37, e2022GB007 658, 2023.

Livestock Improvement Corporation and Dairy NZ: New Zealand Dairy Statistics 2020-21, https://www.lic.co.nz/about/research-publications/dairy-statistics/, 2021.

Manderson, A., Hoogendoorn, C., and Newsome, P.: Grassland improvement mapping using Innovative Data Analysis (IDA) techniques, Manaaki Whenua – Landcare Research, Wellington, New Zealand Manaaki Whenua – Landcare Research Contract Report LC3373, 39, 2019.

Manning, A. J.: The challenge of estimating regional trace gas emissions from atmospheric observations, Philosophical Transactions of the Royal Society A: Mathematical, Physical and Engineering Sciences, 369, 1943–1954, 2011.

McGroddy, M., Baisden, W., and Hedin, L. O.: Stoichiometry of hydrological C, N, and P losses across climate and geology: An environmental matrix approach across New Zealand primary forests, Global Biogeochemical Cycles, 22, 2008.

MfE: LUCAS NZ Land Use Map (v008) [dataset], Ministry for the Environment, 2016.

MfE: Irrigated Land Area [dataset], https://data.mfe.govt.nz/layer/90838-irrigated-land-area-2017/, 2017.

Moore, T.: Dynamics of dissolved organic carbon in forested and disturbed catchments, Westland, New Zealand: 1. Maimai, Water Resources Research, 25, 1321–1330, 1989.

Nickless, A., Rayner, P. J., Engelbrecht, F., Brunke, E.-G., Erni, B., and Scholes, R. J.: Estimates of CO_2 fluxes over the city of Cape Town, South Africa, through Bayesian inverse modelling, Atmospheric Chemistry and Physics Discussions, 2017, 2017.

Ramirez, M. T., Allison, M. A., Bianchi, T. S., Cui, X., Savage, C., Schüller, S. E., Smith, R. W., and Vetter, L.: Modern deposition rates and patterns of organic carbon burial in Fiordland, New Zealand, Geophysical Research Letters, 43, 11–768, 2016.

Rosentreter, J. A., Laruelle, G. G., Bange, H. W., Bianchi, T. S., Busecke, J. J., Cai, W.-J., Eyre, B. D., Forbrich, I., Kwon, E. Y., Maavara, T., et al.: Coastal vegetation and estuaries are collectively a greenhouse gas sink, Nature climate change, pp. 1–9, 2023.

Scott, D. T., Baisden, W. T., Davies-Colley, R., Gomez, B., Hicks, D. M., Page, M. J., Preston, N. J., Trustrum, N. A., Tate, K. R., and Woods, R. A.: Localized erosion affects national carbon budget, Geophysical Research Letters, 33, 2006.

Silvester, W.: Ecological and economic significance of the non-legume symbioses, Proceedings of the 1st International Symposium on Nitrogen-fixation, pp. 489–507, 1976.

Smith, R. W., Bianchi, T. S., Allison, M., Savage, C., and Galy, V.: High rates of organic carbon burial in fjord sediments globally, Nature Geoscience, 8, 450–453, 2015.

Stallard, R. F.: Terrestrial sedimentation and the carbon cycle: Coupling weathering and erosion to carbon burial, Global biogeochemical cycles, 12, 231–257, 1998.

Steinkamp, K., Mikaloff Fletcher, S. E., Brailsford, G., Smale, D., Moore, S., Keller, E. D., Baisden, W. T., Mukai, H., and Stephens, B. B.: Atmospheric CO 2 observations and models suggest strong carbon uptake by forests in New Zealand., Atmospheric Chemistry and Physics, 17, 2017.

Stephens, B., Brailsford, G., Gomez, A., Riedel, K., Fletcher, S. M., Nichol, S., and Manning, M.: Analysis of a 39-year continuous atmospheric CO_2 record from Baring Head, New Zealand, Biogeosciences, 10, 2683, 2013.

Sweeney, C., Gloor, E., Jacobson, A. R., Key, R. M., McKinley, G., Sarmiento, J. L., and Wanninkhof, R.: Constraining global air-sea gas exchange for CO_2 with recent bomb 14C measurements, Global Biogeochemical Cycles, 21, https://doi.org/https://doi.org/10.1029/2006GB002784, 2007.

Tarantola, A.: Inverse problem theory and methods for model parameter estimation, SIAM, 2005.

Uglietti, C., Leuenberger, M. C., and Brunner, D.: European source and sink areas of CO_2 retrieved from Lagrangian transport model interpretation of combined CO_2 and CO_2 measurements at the high alpine research station Jungfraujoch, Atmospheric Chemistry and Physics, 11, 8017–8036, 2011.

Villalobos, Y., Canadell, J. G., Keller, E. D., Briggs, P. R., Bukosa, B., Giltrap, D. L., Harman, I., Hilton, T. W., Kirschbaum, M. U. F., Lauerwald, R., Liang, L. L., Maavara, T., Mikaloff-Fletcher, S. E., Rayner, P. J., Resplandy, L., Rosentreter, J., Metz, E.-M., Serrano, O., and Smith, B.: A Comprehensive Assessment of Anthropogenic and Natural Sources and Sinks of Australasia's Carbon Budget, Global Biogeochemical Cycles, 37, e2023GB007 845, https://doi.org/https://doi.org/10.1029/2023GB007845, e2023GB007845 2023GB007845, 2023.

Walters, D., Boutle, I., Brooks, M., Melvin, T., Stratton, R., Vosper, S., Wells, H., Williams, K., Wood, N., Allen, T., Bushell, A., Copsey, D., Earnshaw, P., Edwards, J., Gross, M., Hardiman, S., Harris, C., Heming, J., Klingaman, N., Levine, R., Manners, J., Martin, G., Milton, S., Mittermaier, M., Morcrette, C., Riddick, T., Roberts, M., Sanchez, C., Selwood, P., Stirling, A., Smith, C., Suri, D., Tennant, W., Vidale, P. L., Wilkinson, J., Willett, M., Woolnough, S., and Xavier, P.: The Met Office Unified Model Global Atmosphere 6.0/6.1 and JULES Global Land 6.0/6.1 configurations, Geoscientific Model Development, 10, 1487–1520, https://doi.org/10.5194/gmd-10-1487-2017, 2017.

Wanninkhof, R.: Relationship between wind speed and gas exchange over the ocean, Journal of Geophysical Research: Oceans, 97, 7373–7382, 1992.

Weiss, R.: Carbon dioxide in water and seawater: the solubility of a non-ideal gas, Marine Chemistry, 2, 203–215, https://doi.org/https://doi.org/10.1016/0304-4203(74)90015-2, 1974.

Weiss, R. and Price, B.: Nitrous oxide solubility in water and seawater, Marine Chemistry, 8, 347–359, 1980.

Wood, N., Staniforth, A., White, A., Allen, T., Diamantakis, M., Gross, M., Melvin, T., Smith, C., Vosper, S., Zerroukat, M., and Thuburn, J.: An inherently mass-conserving semi-implicit semi-Lagrangian discretization of the deep-atmosphere global non-hydrostatic equations, Quarterly Journal of the Royal Meteorological Society, 140, 1505–1520, https://doi.org/https://doi.org/10.1002/qj.2235, 2014.